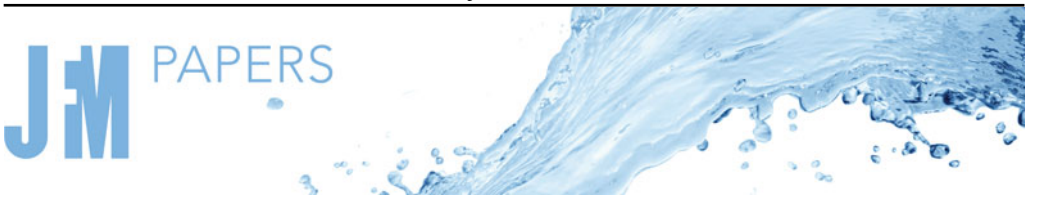
J. Fluid Mech. (2026), *vol.* 1036, A32, doi:10.1017/jfm.2026.11620



Nonlinear development of vortex instabilities over HyTRV lifting body

Ligeng Zhang[1], **Xi Chen**[1] **and Jianqiang Chen**[1]

[1]State Key Laboratory of Aerodynamics, Mianyang, PR China

Corresponding authors: Xi Chen, chenxicoe@pku.edu.cn; Jianqiang Chen, chenjq@cardc.cn

(Received 14 October 2025; revised 15 March 2026; accepted 15 April 2026)

Streamwise vortices are ubiquitous structures on the surfaces of three-dimensional aircrafts and are prone to Z- and Y-mode instabilities. We systematically investigate the nonlinear development of vortex-mode instabilities and resonant interactions employing plane marching nonlinear parabolised stability equations (NPSE3D) and quasi-direct numerical simulation (QDNS). The results suggest the moderately strong subharmonic resonance, and that the detuned interaction between a high-frequency Y-mode and a low-frequency Z-mode may precipitate the transition process. Albeit without any sign of the fundamental resonance, the self-interaction of a Y-mode generates mean flow distortion (MFD) that, in turn, yields the amplitude saturation and causes the hairpin vortex formed by the Y-mode to cascade into smaller scale vortices via vortex reconnection. Sensitivity analysis reveals that MFD exerts a destabilising direct effect on modal instability, but this is offset by its stabilising indirect effect through weakened base-flow shear, ultimately resulting in net stabilisation. Higher-frequency modes display heightened sensitivity to MFD. Moreover, QDNS exhibits a late-stage surface skin friction overshoot, accompanied by an amplification of subharmonic frequencies.

Key words: high-speed flow, nonlinear instability, transition to turbulence

1. Introduction

The issue of boundary layer transition has long been a significant yet challenging research topic. With the ongoing advancement of high-speed flight technology, comprehending the boundary layer transition mechanism becomes crucially important, since the boundary layer transition can yield a substantial rise in wall friction and thermal load.

© The Author(s), 2026. Published by Cambridge University Press.

https://doi.org/10.1017/jfm.2026.11620 Published online by Cambridge University Press

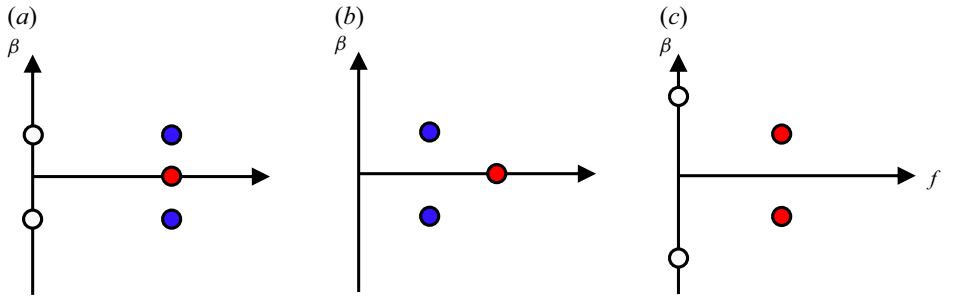


Figure 1. Distributions of primary and secondary disturbance frequencies and wavenumbers in (*a*) the fundamental resonance of the K-type transition, (*b*) the subharmonic resonance of the N-type transition and (*c*) the O-type transition. The red, blue and white symbols denote the primary modes, travelling secondary modes and stationary streaks, respectively.

The transition paths and mechanisms of boundary layers are highly diverse, influenced significantly by the amplitude of incoming flow disturbances. Early studies (Herbert 1988; Kachanov 1994; Schmid & Henningson 2012) predominantly centred on incompressible boundary layers, unveiling a variety of transition scenarios. Figure 1 illustrates the schematic diagram of the frequencies and wavenumbers for the weakly nonlinear transition mechanisms of three representative scenarios. These categories correspond to different nonlinear interaction mechanisms involving a pair of oblique waves with the opposite wave angles and/or a planar wave.

For supersonic flows, the oblique first mode is most unstable, leading to a strong oblique breakdown constituted by a pair of oblique first modes (Chang & Malik 1994). In the high-Mach-number regime, the planar Mack second mode dominates, favouring both the fundamental resonance (Sivasubramanian & Fasel 2015) and the combination resonance (Chen, Zhu & Lee 2017). By contrast, subharmonic resonance is generally considered to be relatively weak. Additionally, the interaction between the oblique second mode and oblique waves can facilitate energy transfer via the parametric resonance process of difference modes (Zhou *et al.* 2023). Furthermore, the coupling of multiple dominant modes can also accelerate the transition process through interactions involving higher harmonics (Jahanbakhshi & Zaki 2019; Guo, Hao & Wen 2023).

Compared with the two-dimensional (2-D) counterpart, three-dimensional (3-D) boundary layers feature three specific regions, i.e. the attachment-line, cross-flow and streamwise vortex regions, owing to the azimuthal pressure gradient (Chen *et al.* 2022). For supersonic boundary layers, the attachment line region exhibits instability modes similar to those of two-dimensional boundary layers (Fedorov & Egorov 2022). A recent study (Chen *et al.* 2023) demonstrates global Mack modes can spontaneously trigger the fundamental resonance. The cross-flow region is susceptible to cross-flow instability disturbances that, with sufficiently large amplitudes, are prone to secondary instabilities responsible for the final breakdown of the boundary layer (Craig & Saric 2016; Moyes *et al.* 2017; Xu *et al.* 2019). Recently, Ren & Kloker (2022) analysed cross-flow instabilities in non-ideal gases, finding that wall heating destabilises cross-flow instabilities in the supercritical regime, whereas the supercritical and subcritical regimes show opposite wall-temperature effects relative to ideal gases and liquids. Similarly, the streamwise vortex region features a (pair of) large-scale streamwise vortex (vortices) accompanied by low-speed streaky structures in the base flow, as illustrated in figure 2. This region, generally coinciding with the low-pressure region, emerges inevitably on almost all three-dimensional vehicles, like inclined cones with non-zero angle of attacks (Chen *et al.* 2020;

https://doi.org/10.1017/jfm.2026.11620 Published online by Cambridge University Press

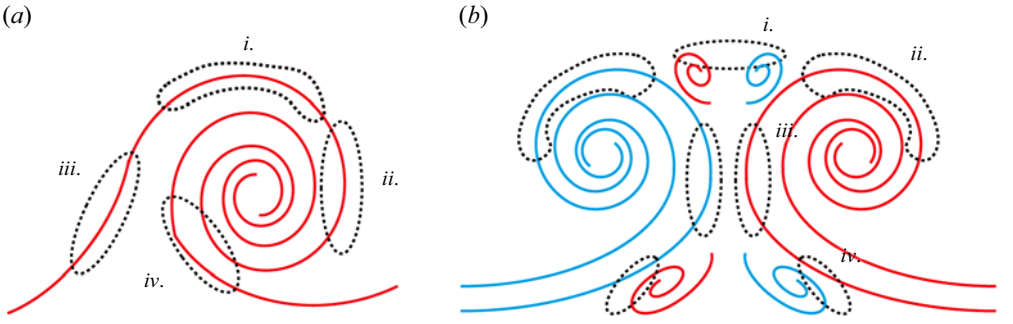


Figure 2. Illustrations of the vortex structures and stability distributions for two representative streamwise vortices: (*a*) asymmetric streamwise vortex and (*b*) symmetric vortex. The black dashed circles denote the regions of modal instability, namely (i, ii) the wall-normal shear layer and (iii, iv) the lateral shear layer.

Li *et al.* 2020*b*; Paredes *et al.* 2021; Zhang *et al.* 2022), elliptic cones (Huntley & Smits 2000; Paredes *et al.* 2016), finned cone (Mullen *et al.* 2019; Turbeville & Schneider 2019; Peck, Groot & Reed 2024; Araya *et al.* 2025), the BOLT (BOundary Layer Transition flight-test vehicle) (Wheaton *et al.* 2018; Thome, Knutson & Candler 2019; Li *et al.* 2020*a*; Kostak & Bowersox 2021), the HyTRV lifting body (Chen *et al.* 2022; Yang, Li & Liu 2025; Zhang *et al.* 2025) and a capsule configuration with distributed roughnesses (Di Giovanni & Stemmer 2018). The linear instability characteristics of the streamwise vortex region have become increasingly clear. The streamwise vortex usually forms an lateral high-shear layer and an wall-normal high-shear layer that could support Z- and Y-modes, respectively (Wassermann & Kloker 2002). Additionally, a second Mack mode can also be identified and may morph into the aforementioned shear-layer instabilities downstream (Li *et al.* 2020*a*; Zhang *et al.* 2022).

The nonlinear breakdown process of streamwise vortices in 3-D boundary layers has also been documented by a few studies (Hiejima 2017; Wang *et al.* 2017; Di Giovanni & Stemmer 2018; Hartman, Hader & Fasel 2021; Tufts *et al.* 2022; Wang *et al.* 2023) relying exclusively on direct numerical simulations, which is characterised by regular hairpin structures followed by hairpin wave-packets. Similar coherent structures have also been observed in the late transition stage of cross-flow vortices (Wassermann & Kloker 2003; Bonfigli & Kloker 2007; Li, Choudhari & Duan 2017; Chen *et al.* 2021; Su, Li & Han 2024) as well as Görtler vortices (Chen, Huang & Lee 2019; Li, Choudhari & Paredes 2022), implying that they are omnipresent in the transition process of the wall-bounded streamwise vortices. However, the underlying nonlinear transition mechanisms remain largely unknown.

This paper aims to shed light on nonlinear transition mechanisms underlying the breakdown process of streamwise vortices using the nonlinear plane-marching parabolised stability equations (NPSE3D) in combination with direct numerical simulation (DNS), sensitivity and energy transfer analyses. By leveraging the separating scale of the fast varying small-amplitude disturbances and the slowly varying base flow in the streamwise direction, the NPSE3D method turns out to be a very efficient tool, capable of adequately resolving the weakly nonlinear development of a single mode as well as nonlinear interactions of modes (Paredes *et al.* 2017, 2019; Chen *et al.* 2023; Wang *et al.* 2024). We attempt to answer whether resonance mechanisms similar to those in two-dimensional boundary layers are still active in the present 3-D case and how the instability modes modulate the base flow, causing the rise of the surface friction and heat transfer. Moreover, we also try to establish the relationship between the nonlinear evolving instability modes

https://doi.org/10.1017/jfm.2026.11620 Published online by Cambridge University Press

Angle of attack	Mach number (Ma_∞)	Unit Reynolds number (Re^*_∞)	Static temperature (T^*_e)	Wall temperature (T^*_w)
2°	6	1×10^7 m^{-1}	79 K	300 K

Table 1. Flow conditions.

and the coherent structures. Following our prior research (Chen *et al.* 2022), this study focuses on the shoulder vortex of the HyTRV lifting body. The remainder of this paper is organised as follows: § 2 presents the numerical methodology and theoretical framework for stability analysis. Section 3 details the linear stability results complemented by an energy transfer analysis. Section 4 provides a comprehensive investigation of the transition mechanisms through nonlinear analyses, including the impact of the mean-flow distortion (MFD) and the sensitivity of the vortex modes. Vortex breakdown simulations are presented in § 5, and the conclusions are summarised in § 6.

2. Numerical set-up and methodology

2.1. *Geometry and flow conditions*

The HyTRV model is specifically designed to investigate the transition mechanisms of 3-D boundary layers over high-speed vehicles. Its nose is an elliptic cone with an aspect ratio of 2 : 1. The body cross-section is generated separately on the windward and leeward sides. The windward part is an aspect ratio 4 : 1 elliptic cone, while the leeward part is a linear combination of a class function, and shape function transformation technique (CST) curve and an aspect ratio 4 : 1 elliptic curve. For a detailed description of the HyTRV model geometry, readers are referred to Liu *et al.* (2021). Two coordinate systems are involved in this study. The first is the Cartesian coordinate system (X, Y, Z) and the second is the body-oriented coordinate system (ξ, η, ζ), corresponding to the streamwise, azimuthal and wall-normal directions, respectively. The azimuth angle is defined as $\theta \equiv \arctan(Y/Z)$, ranging from the upper centreline ($\theta = 0°$) to the bottom centreline ($\theta = 180°$). The flow condition considered in this research refers to a typical wind tunnel condition (Chen *et al.* 2022), which is summarised in table 1.

2.2. *Base flow calculations*

The numerical simulation is carried out using the parallel computational fluid dynamics software OPENCFD, developed by Li, Fu & Ma (2008). The base flow calculations are performed in two distinct stages. Initially, a second-order accurate scheme is used to compute the steady laminar flow throughout the entire domain. This computed flow field subsequently provides the inlet boundary condition for the second stage, which focuses on a smaller near-wall region downstream of the nose. In the latter stage, the grid configuration consists of 520, 741 and 241 nodes in the streamwise, azimuthal and wall-normal directions, respectively. The grid resolution is refined in areas where vortical structures are anticipated to develop and turns out to be sufficient to obtain converged results, as shown in Appendix B. Given the symmetry of the geometry, only half of it is considered in the simulations. The convective and viscous terms are discretised using a fifth-order accurate upwind scheme and a sixth-order accurate central difference scheme, respectively.

Figure 3(*a*) provides an overview of the base flow characteristics. Notably, vortical structures spontaneously develop over the windward surface and the shoulder region as

https://doi.org/10.1017/jfm.2026.11620 Published online by Cambridge University Press

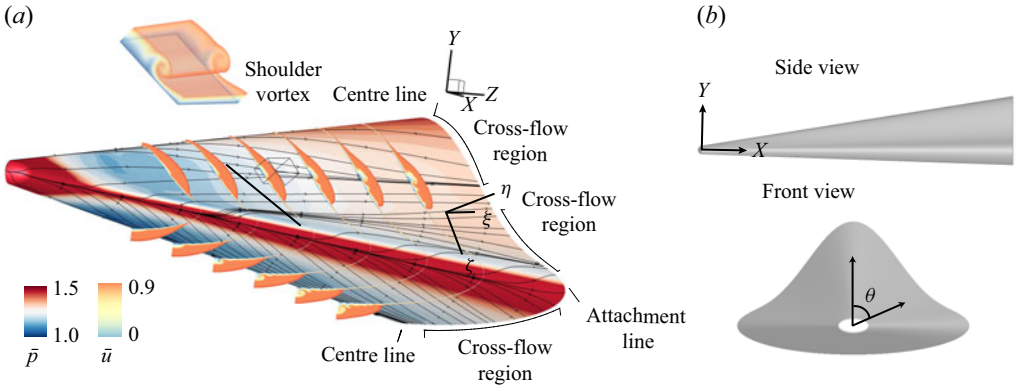


Figure 3. (*a*) Base flow for stability analysis, and (*b*) front and side views of the HyTRV model.

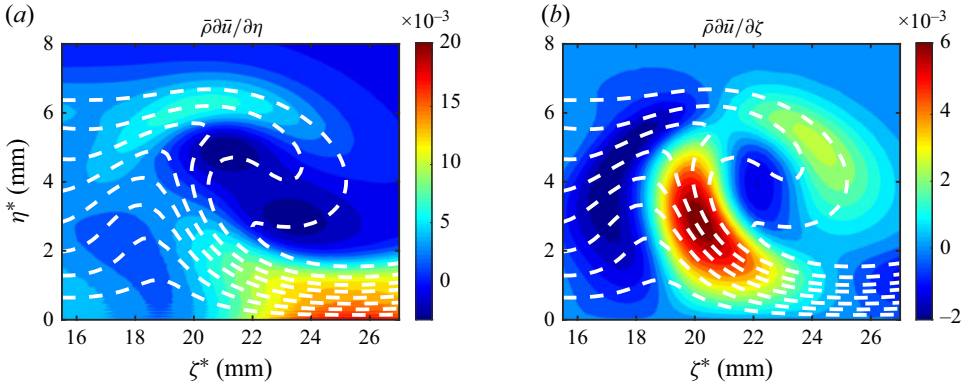


Figure 4. Normalised streamwise velocity profile (displayed in white dashed lines) and the shear layer, namely $\bar{\rho}\partial\bar{u}/\partial\eta$ and $\bar{\rho}\partial\bar{u}/\partial\zeta$, of the profile at $X^* = 700$ mm.

a result of the azimuthal pressure gradient. In contrast to the symmetric windward vortex, the shoulder vortex exhibits an asymmetrical structure, resembling a single cross-flow vortex. Figure 4 illustrates the wall-normal and azimuthal shears of the basic state at a representative station ($X^* = 700$ mm, the dimensional variables are denoted with the superscript.). Two high-shear layers are evident, located at the top and root of the vortex. As will be elaborated in the subsequent section, the unstable modes are closely linked to these shear regions.

2.3. *Multi-dimensional stability analysis theories*

With the parallel-flow assumption, the flow field may be represented as the sum of the base flow and a fluctuating quantity as

$$\boldsymbol{q}(\xi, \eta, \zeta, t) = \bar{\boldsymbol{q}} + \tilde{\boldsymbol{q}} = \bar{\boldsymbol{q}}(\eta, \zeta) + \hat{\boldsymbol{q}}(\eta, \zeta)\exp(i\alpha\xi - i\omega t) + c.c., \tag{2.1}$$

where $\boldsymbol{q}$ represents flow quantities, namely velocities, u, v, w, pressure p and temperature T; $\bar{\boldsymbol{q}}$ denotes the undisturbed flow field, $\tilde{\boldsymbol{q}}$ refers to the unsteady, sufficiently small perturbations in the flow field, $\hat{\boldsymbol{q}}$ denotes the function of the shape of the disturbance; α the number of streamwise waves; and ω the angular frequency with the corresponding frequency denoted by f. Here, $c.c$ refers to the complex conjugate. Substituting this

https://doi.org/10.1017/jfm.2026.11620 Published online by Cambridge University Press

decomposition into the Navier–Stokes equations, subtracting the undisturbed equation, and neglecting the nonlinear and non-parallel terms yields the 2-D eigenvalue problem (BiGlobal) as

$$\mathcal{A}\boldsymbol{\phi} = \alpha\mathcal{B}\boldsymbol{\phi}, \tag{2.2}$$

where $\boldsymbol{\phi}$ denote $[\hat{\boldsymbol{q}}; \alpha\hat{\boldsymbol{q}}]$. Here, α is assumed to be a complex number, while ω is a real number. The entries of operators $\mathcal{A}$ and $\mathcal{B}$ are detailed by Chen *et al.* (2022).

The parallel-flow assumption in BiGlobal analysis is relaxed in the plane-marching parabolised stability equations (PSE3D) in which the flow field can be decomposed as

$$\boldsymbol{q}(\xi, \eta, \zeta, t) = \bar{\boldsymbol{q}}(\xi, \eta, \zeta) + \sum_{n=0}^{N} \hat{\boldsymbol{q}}_n(\xi, \eta, \zeta) \exp\left(i \int_{\xi} \alpha_n \mathrm{d}\xi - in\omega t\right) + c.c., \tag{2.3}$$

where $\bar{\boldsymbol{q}}(\xi, \eta, \zeta)$ varies slowly with respect to ξ. Substituting (2.3) into Navier–Stokes equations and neglecting higher order derivatives of $\hat{\boldsymbol{q}}_n$ with respect to ξ lead to the nonlinear plane-marching parabolised stability equations (NPSE3D) as

$$\mathcal{L}_n\hat{\boldsymbol{q}}_n + \mathcal{M}_n\frac{\partial\hat{\boldsymbol{q}}_n}{\partial\xi} = \mathcal{F}_n, \tag{2.4}$$

where $\mathcal{F}_n$ is the nonlinear forcing part for mode with angular frequency $n\omega$. It turns out that the harmonics of modes (q_n, $n > 1$) exert little effects on the nonlinear development of the primary mode (not shown here) and are thus neglected in this paper for simplicity. The detailed description for coefficient matrices $\mathcal{L}_n$ and $\mathcal{M}_n$ can be found from Chen *et al.* (2022). When neglecting the nonlinear forcing term, we get linear plane-marching parabolised stability equations (LPSE3D) that study the linear development of a single mode. The initial disturbance profiles for the calculations are obtained from BiGlobal. The eigenfunction from the BiGlobal analysis at the upstream location serves as the initial amplitude function for the parabolised disturbance equations, while the local wavenumber provides the starting value for the streamwise marching. The grid used in the multi-dimensional stability analysis is refined at the wall where the main body of the streamwise vortex resides. To reduce the computational cost and ensure that the perturbation amplitude drops to zero in the far field, we adopt a sparse setting in the upper and side-band regions of the grid. No-slip and isothermal boundary conditions are imposed at the wall. Homogeneous boundary conditions are used, except for pressure, in both BiGlobal and PSE3D methods, assuming that the disturbance concentrates on the vortex region with vanishing amplitudes on the lateral boundaries. The grid resolution of 200×150 in the azimuthal and wall-normal directions is employed for both BiGlobal and LPSE3D/NPSE3D analyses, which has been demonstrated to be sufficient in the prior study (Chen *et al.* 2022). The convergence of the LPSE3D/NPSE3D solutions with respect to the iteration step length is verified.

2.4. *Energy transfer analysis*

The underlying growth mechanisms of the mode can be readily characterised by the energy transfer equation (Malik *et al.* 1999; Chen *et al.* 2023). The disturbance form given in (2.1) is composed as $\tilde{\boldsymbol{q}} = [\tilde{u}, \tilde{v}, \tilde{\rho}, \tilde{T}, \tilde{w}]^T$. Accordingly, the energy norm (Chu 1965) can be expressed as

$$\tilde{\mathcal{E}} = \iint_{\Omega} \tilde{E}\,\mathrm{d}\zeta\,\mathrm{d}\eta = \iint_{\Omega} \tilde{\boldsymbol{q}}^H \boldsymbol{M}_E \tilde{\boldsymbol{q}}\,\mathrm{d}\zeta\,\mathrm{d}\eta, \tag{2.5}$$

https://doi.org/10.1017/jfm.2026.11620 Published online by Cambridge University Press

where the $\boldsymbol{M}_E$ takes the form of

$$\boldsymbol{M}_E = diag\left[\bar{\rho}, \bar{\rho}, \frac{\bar{T}}{\bar{\rho}\gamma Ma_\infty^2}, \frac{\bar{\rho}}{\gamma(\gamma-1)\bar{T}Ma_\infty^2}, \bar{\rho}\right]. \tag{2.6}$$

The governing equation for perturbation energy can be written as follows

$$\frac{\mathrm{D}\tilde{E}}{\mathrm{D}t} = \mathcal{L} + \mathcal{N}, \quad \mathcal{L} = \mathcal{P}_y + \mathcal{P}_z + \mathcal{P}_\varepsilon + \Pi + \Xi + \mathcal{V}, \tag{2.7}$$

where P_y and P_z are production terms pertaining to the wall-normal and lateral derivatives of the streamwise base velocity, and P_ε denotes the sum of the other production terms. The rest of the terms stand for non-parallel effects (Ξ), pressure work (Π), viscous effects ($\mathcal{V}$) and nonlinear terms ($\mathcal{N}$). The streamwise growth rate of the disturbance energy σ_E can be decomposed by integrating the disturbance streamwise energy flux as

$$\sigma_E = \sigma_\mathcal{L} + \sigma_\mathcal{N} = \frac{1}{\hat{\mathcal{E}}}\left[\iint_\Omega \left(P_y + P_z + P_\varepsilon + \Xi + \Pi + \mathcal{V}\right)\,\mathrm{d}\zeta\,\mathrm{d}\eta + \iint_\Omega \mathcal{N}\mathrm{d}\zeta\,\mathrm{d}\eta\right]. \tag{2.8}$$

The total production can be further decomposed as $\mathcal{P} = P_y + P_z + P_\varepsilon = P_{ij} + P_{Ti} + P_{Ri}$, which is rewritten as

$$\mathcal{P} = \underbrace{\bar{\rho}\tilde{u}^+\tilde{v}\frac{\partial\bar{u}}{\partial\eta}}_{P_y} + \underbrace{\bar{\rho}\tilde{u}^+\tilde{w}\frac{\partial\bar{u}}{\partial\zeta}}_{P_z} + \underbrace{\overbrace{\bar{\rho}\tilde{u}_i^+\tilde{u}_j\frac{\partial\bar{u}_i}{\partial n_j}}^{i\&j=2,3} + \overbrace{\frac{\bar{\rho}}{\gamma(\gamma-1)Ma_\infty^2\bar{T}}\tilde{T}^+\tilde{u}_i\frac{\partial\bar{T}}{\partial n_i}}^{P_{Ti}} + \overbrace{\frac{\bar{T}}{\gamma Ma_\infty^2\bar{\rho}}\tilde{\rho}^+\tilde{u}_i\frac{\partial\bar{\rho}}{\partial n_i}}^{P_{Ri}}}_{P_\varepsilon}, \tag{2.9}$$

where $(n_i)_{i=1,2,3} = (\xi, \eta, \zeta)$. The superscript $^+$ denotes the conjugate. Here, each component of $\mathcal{P}$ denotes the energy source terms associated with different components of mean flow shear. For example, P_{12} corresponds to the normal shear term of streamwise velocity $\partial\bar{u}/\partial\eta$, P_{23} represents the lateral shear term of normal velocity $\partial\bar{v}/\partial\zeta$ and P_{T2} pertains to the wall-normal shear term of temperature $\partial\bar{T}/\partial\eta$.

The nonlinear energy transport σ_N arises from the interactions among disturbances. In the NPSE3D framework, this quantity incorporates both stationary terms (MFD) and the travelling terms. Consequently, the nonlinear energy transport can be decomposed into two distinct components as

$$\sigma_N = \sigma_{\mathcal{N}_{others}} + \sigma_{\mathcal{N}_{mfd}}, \tag{2.10}$$

where $\sigma_{\mathcal{N}_{mfd}}$ quantifies direct MFD contributions and $\sigma_{\mathcal{N}_{others}}$ represents the energy transfer directly induced by the nonlinear forcing from other Fourier modes.

2.5. *Sensitivity analysis*

One of key characteristic of the nonlinear transition stage is the modification of the base flow due to nonlinear interaction of instability modes. Therefore, comprehending how changes in the mean flow field influence streamwise vortex modes can shed light on the potential role of nonlinear processes in the early nonlinear stages of streamwise vortex instability. By introducing the adjoint equations (Park & Zaki 2019; Guo *et al.* 2023; Ren *et al.* 2025), we can readily obtain how the eigenvalues of the unstable modes shift due to the base flow distortion. The perturbed eigenvalue equation in the presence of a base flow

https://doi.org/10.1017/jfm.2026.11620 Published online by Cambridge University Press

perturbation quantity δQ can be written as

$$\left(\mathcal{A}+\frac{\partial \mathcal{A}}{\partial Q}\delta Q\right)(\boldsymbol{\phi}+\delta\boldsymbol{\phi})=(\alpha+\delta\alpha)\left(\mathcal{B}+\frac{\partial \mathcal{B}}{\partial Q}\delta Q\right)(\boldsymbol{\phi}+\delta\boldsymbol{\phi}). \tag{2.11}$$

The equation then yields

$$\mathcal{A}\boldsymbol{\phi}+\mathcal{A}\delta\boldsymbol{\phi}+\frac{\partial \mathcal{A}}{\partial Q}\delta Q\,\boldsymbol{\phi}=\alpha\mathcal{B}\boldsymbol{\phi}+\alpha\mathcal{B}\delta\boldsymbol{\phi}+\alpha\frac{\partial \mathcal{B}}{\partial Q}\delta Q\,\boldsymbol{\phi}+\delta\alpha\,\mathcal{B}\boldsymbol{\phi}+\mathcal{O}(\delta^2). \tag{2.12}$$

Subsequently, by subtracting the zeroth-order equation and neglecting the second-order infinitesimals $O(\delta^2)$, the equation is transformed into

$$(\mathcal{A}-\alpha\mathcal{B})\delta\boldsymbol{\phi}=\left(-\frac{\partial \mathcal{A}}{\partial Q}+\alpha\frac{\partial \mathcal{B}}{\partial Q}\right)\delta Q\boldsymbol{\phi}+\delta\alpha\mathcal{B}\boldsymbol{\phi}. \tag{2.13}$$

The left-hand side term of the equation can be eliminated using the adjoint mode $\boldsymbol{\phi}^\dagger$, where the dagger symbol (†) denotes the adjoint mode which satisfies the adjoint relation as

$$\left(\boldsymbol{\phi}^\dagger,(\mathcal{A}-\alpha\mathcal{B})\boldsymbol{\phi}\right)=\left((\mathcal{A}^\dagger-\alpha^\dagger\mathcal{B}^\dagger)\boldsymbol{\phi}^\dagger,\boldsymbol{\phi}\right)=0. \tag{2.14}$$

Note that (a,b) represent $\int_\Omega a^+ b\,\mathrm{d}\Omega$, representing the integral in the computational domain, where $^+$ represent the complex conjugate. The inner product of the adjoint mode and (2.13) yields

$$0=\left(\boldsymbol{\phi}^\dagger,\left(-\frac{\partial \mathcal{A}}{\partial Q}+\alpha\frac{\partial \mathcal{B}}{\partial Q}\right)\boldsymbol{\phi}\delta Q+\delta\alpha\mathcal{B}\boldsymbol{\phi}\right). \tag{2.15}$$

After rearranging, the following can be derived:

$$\delta\alpha\left(\boldsymbol{\phi}^\dagger,-\mathcal{B}\boldsymbol{\phi}\right)=\left(\boldsymbol{\phi}^\dagger,\left(\frac{\partial \mathcal{A}}{\partial Q}\delta Q-\alpha\frac{\partial \mathcal{B}}{\partial Q}\delta Q\right)\boldsymbol{\phi}\right), \tag{2.16}$$

where the right-hand side term of the equation can be expressed as $(\hat{\mathcal{S}},\delta Q)$. Here, $\hat{\mathcal{S}}$ represents the sensitivity distribution of any variable Q (denoted as $\bigtriangledown_Q\alpha$), which reads

$$\hat{\mathcal{S}}=\left(\boldsymbol{\phi}^\dagger,\left(\frac{\partial \mathcal{A}}{\partial Q}-\alpha\frac{\partial \mathcal{B}}{\partial Q}\right)\boldsymbol{\phi}\right)\Big/(\boldsymbol{\phi}^\dagger,-\mathcal{B}\boldsymbol{\phi}). \tag{2.17}$$

3. Linear modal analysis

The linear stability characteristics of the shoulder vortex, including the eigenvalue spectrum and spatial linear evolution, were comprehensively investigated in our prior work (Chen *et al.* 2022). Herein, we succinctly summarise the key features for subsequent analyses. Figure 5 illustrates a representative vortex instability spectrum obtained via BiGlobal analysis at a specific streamwise location ($X^*=700$ mm). For clarity, modes located at the top of the vortex are denoted as 'Y', while the modes at the root are labelled as 'Z'. These modes are ranked according to their amplification rates. Each shape function pattern corresponds to the mode at its most amplified frequencies (namely mode Y1 with 76 kHz, Y2 with 50 kHz, Z1 with 13 kHz and Z2 with 10 kHz). The spectrum consists of two Y-modes and two Z-modes, all of which exhibit peak amplitudes at their respective critical layers.

Figure 6(*a*,*b*) presents the disturbance energy budget for the dominant Y-(Y1) and Z-(Z1) modes. Specifically, the Y-mode derives its energy predominantly from the wall-normal production term, while the Z1 mode acquires energy mainly from the lateral production term; based on this distinct energy sourcing mechanism. Although these Z and

https://doi.org/10.1017/jfm.2026.11620 Published online by Cambridge University Press

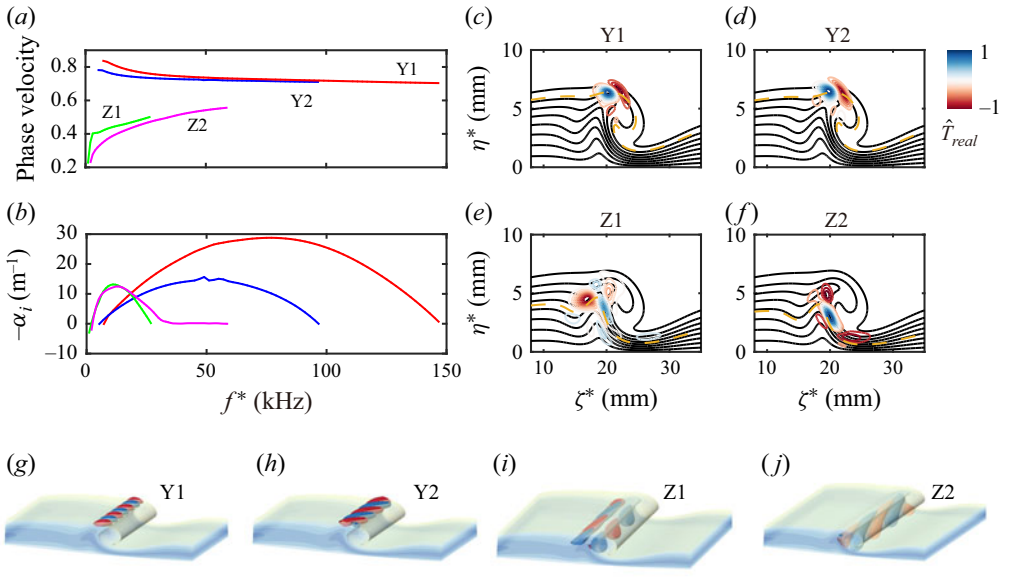


Figure 5. (*a*,*b*) Phase velocities and growth rates of modes as a function of frequency for shoulder vortex at a representative streamwise location, $X^* = 700$ mm. (*c*–*f*) Shape functions together with the streamwise base flow contour of $\bar{u} = 0.1 : 0.1 : 0.8$. (*g*–*j*) Reconstructed spacial structures of the modes.

Y modes bear resemblance to the Y-mode and Z-mode in cross-flow-dominated boundary layers (Malik *et al.* 1999; Bonfigli & Kloker 2007), notable differences exist in terms of frequency ranges, amplification rates and phase velocities. Particularly in the present case, the Y modes exhibit a broader frequency range, higher amplification rates and higher phase velocities compared with the Z modes, while Z-mode and Y-mode disturbances of cross-flow vortices may possess comparable frequency ranges and phase velocities. Figure 6(*c*,*d*) illustrate the normalised contributions of energy production terms for the two modes across various frequencies. Notably, the contributions of temperature and density gradients to the energy budget are substantially higher for the Y1 mode than for the Z1 mode.

Figure 7 presents the N-factor curves at various frequencies, calculated using LPSE3D starting from the near-neutral points of each mode; these near-neutral points were identified through an iterative method (Moyes *et al.* 2019; Zhang *et al.* 2022). Clearly, the Y1 mode is most unstable, followed by the Y2, Z1 and Z2 modes. Distinct high-frequency Y1 mode unstable region and low-frequency Z1 mode instability region can be easily observed in the N-factor contour plot, with the most amplified frequency around 90 kHz.

4. Nonlinear development and interactions of vortex modes

In this section, we conduct a systematic parametric study using NPSE3D to investigate the nonlinear development of vortex modes. Specifically, we aim to evaluate whether classical secondary instabilities – including fundamental, subharmonic and combination resonances, well-documented in two-dimensional boundary layers – are also active in the present three-dimensional configuration. For this purpose, three groups of test cases are designed, as detailed in table 2. Group A investigates the self-interaction of the Y1 mode, as well as the potential fundamental resonance that may arise simultaneously during the

https://doi.org/10.1017/jfm.2026.11620 Published online by Cambridge University Press

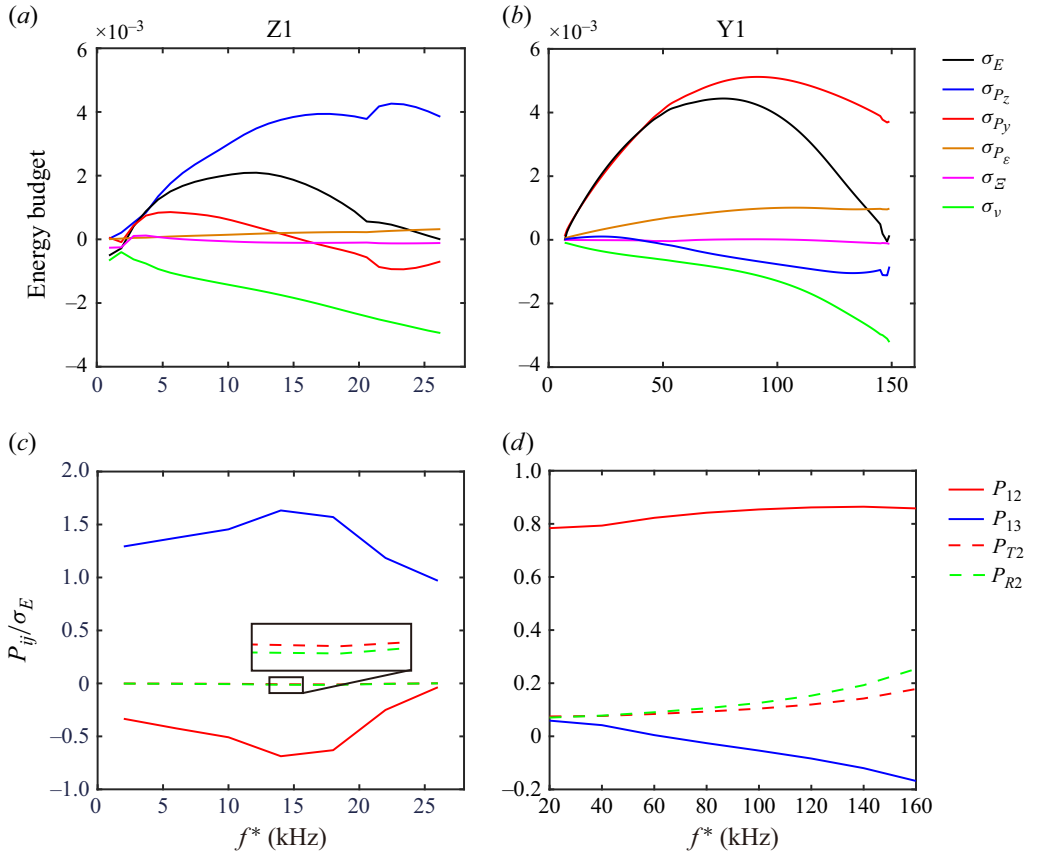


Figure 6. Energy budget decomposition of (*a*) mode Z1 and (*b*) mode Y1 at $X^* = 700$ mm, with (*c*,*d*) the most important four normalised production components.

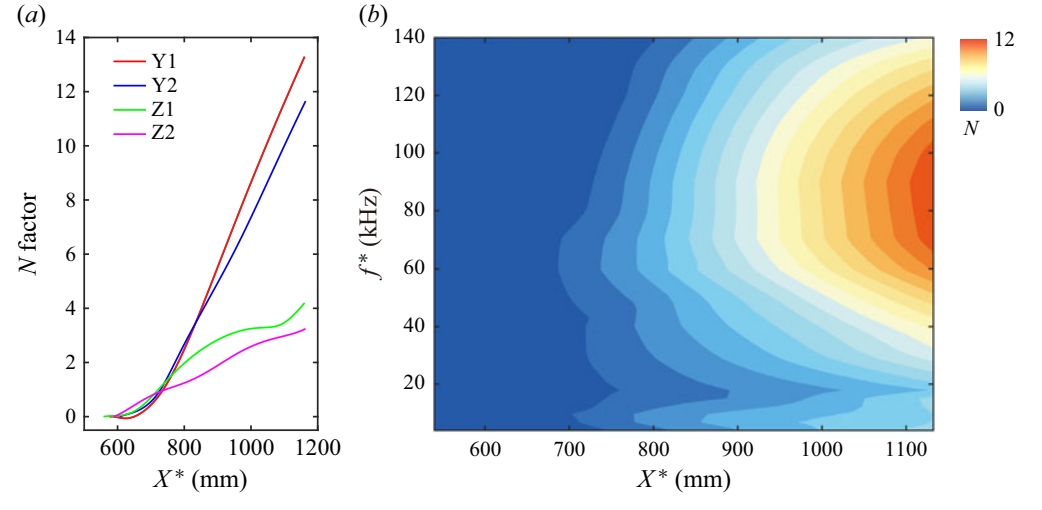


Figure 7. (*a*) N factors obtained by LPSE3D initiated at the near-neutral points of each mode and (*b*) N-factor contour in the X–f plane.

https://doi.org/10.1017/jfm.2026.11620 Published online by Cambridge University Press

Case	Mode type	f^* (kHz)	Initial amplitude
A1	(Y1)	(10−140)	(10^{-4})
B1	(Y2,Y1)	(45, 90)	$(10^{-5}, 10^{-4})$
B2	(Y1,Y1)	(45, 90)	$(10^{-5}, 10^{-4})$
C1	(Z1,Y1)	(10, 70)	$(10^{-4}, 10^{-4})$
C2	(Z1,Y1)	(10, 70)	$(10^{-2}, 10^{-4})$

Table 2. Initial computational settings used in NPSE3D analysis.

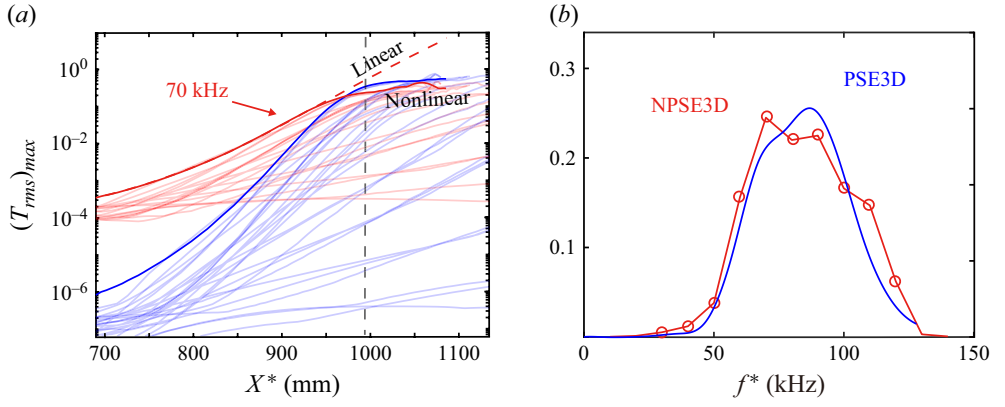


Figure 8. (*a*) NPSE3D analysis of mode Y1 in a wide frequency range. The primary mode is marked as red and the nonlinear generated MFD is marked as blue. The most amplified frequency is 70 kHz, as illustrated in the figure. (*b*) Comparison of amplitude spectrum at $X^* = 1000$ mm obtained by LPSE3D and NPSE3D.

self-interaction process (Chen *et al.* 2023). Group B focuses specifically on the potential subharmonic resonance. Group C examines the detuned interactions between the Y- and Z- modes as well as the potential combination resonance with a more general frequency relationship (neither harmonic nor subharmonic). Note that the primary modes in groups A and B belong to the Y1 mode instability since it represents the most unstable mode in the present case.

4.1. *Fundamental interactions*

In this section, we first examine the self-interaction of the disturbance. To simplify the calculation, the NPSE3D simulation includes only one primary frequency and the nonlinearly generated MFD. The NPSE3D calculations initiate at the near-neutral point of each mode, with the inlet disturbance temperature amplitude of 0.0001.

Figure 8 depicts the evolution of the Y1 mode at multiple frequencies. Under the influence of MFD, the modal amplitude exhibits a suppressed growth rate compared with the linear case, while saturation occurs at approximately the same amplitude across all frequencies. Notably, the saturation amplitude for temperature disturbances of the primary mode approaches 0.3. No significant secondary amplitude growth is observed, indicative of the absence of fundamental resonance. This behaviour contrasts sharply with findings by Chen *et al.* (2023) in a three-dimensional attachment-line boundary layer study, where the Mack mode triggers fundamental resonance prior to nonlinear saturation, inducing rapid growth of MFD and streaky structures. Notably, the Z1 mode also exhibits

https://doi.org/10.1017/jfm.2026.11620 Published online by Cambridge University Press

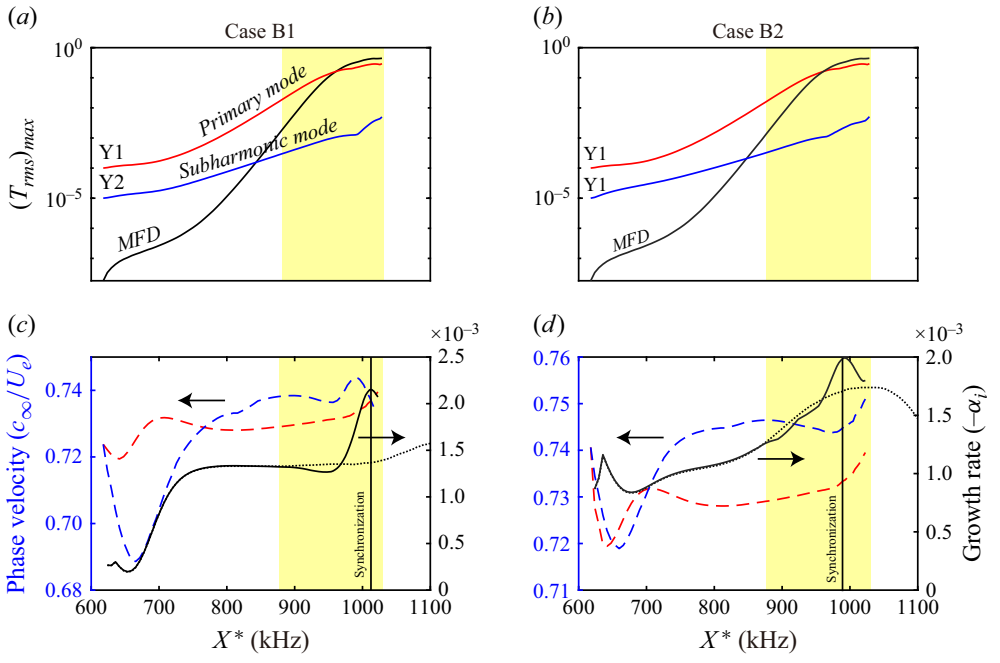


Figure 9. (*a*,*b*) Maxima temperature amplitude evolution process along the streamwise direction for the interaction between the Y1 mode at 90 kHz and the subharmonic mode (45 kHz): Y2 mode for case B1 and Y1 mode for case B2. The phase velocities of the primary wave and subharmonic wave in (*c*) case B1 and (*d*) case B2, are shown by red and blue dashed lines, respectively. The growth rates of the subharmonic mode are indicated by black solid and dotted lines, with the dotted line representing the linear case.

a consistent saturation amplitude during the nonlinear stage. Its overall saturation process remains unchanged regardless of the initial amplitude. Additionally, the self-interaction slightly lowers the peak frequency of vortex instabilities, as shown in figure 8(*b*), which will be further explored in § 4.4.

4.2. *Subharmonic interactions*

Subharmonic resonance is one of the most efficient secondary-instability mechanisms in the low-speed regime (Herbert 1988; Kachanov 1994), yet appears to be less prominent in hypersonic flows (Sivasubramanian & Fasel 2014; Chen *et al.* 2017). To examine whether subharmonic-resonance-like interactions are active in the present 3-D configuration, we investigate the nonlinear interactions between the fundamental Y1 mode (90 kHz) and the nominally subharmonic Y1/Y2 mode (45 kHz) in cases B1 and B2. It is important to note that the choice of frequency here does not qualitatively affect the results of the subharmonic resonance discussed in this subsection.

Figure 9(*a*,*b*) reveal that both cases B1 and B2 exhibit moderate secondary growth in their subharmonic modes. The amplitude evolution features a pronounced inflection point near $X^* = 950$ mm, which coincides with abrupt variations in phase velocity (as shown by the dashed lines in figure 9*c*,*d*), thereby suggesting the occurrence of mode synchronisation.

Figure 10(*a*) decomposes the total growth rate (σ_E) into linear ($\sigma_{\mathcal{L}}$) and nonlinear ($\sigma_{\mathcal{N}_{mfd}}$, $\sigma_{\mathcal{N}_{others}}$) components for case B1. The results of case B2 exhibit a comparable trend and are therefore omitted for brevity. Notably, the increase in the growth rate of the subharmonic

https://doi.org/10.1017/jfm.2026.11620 Published online by Cambridge University Press

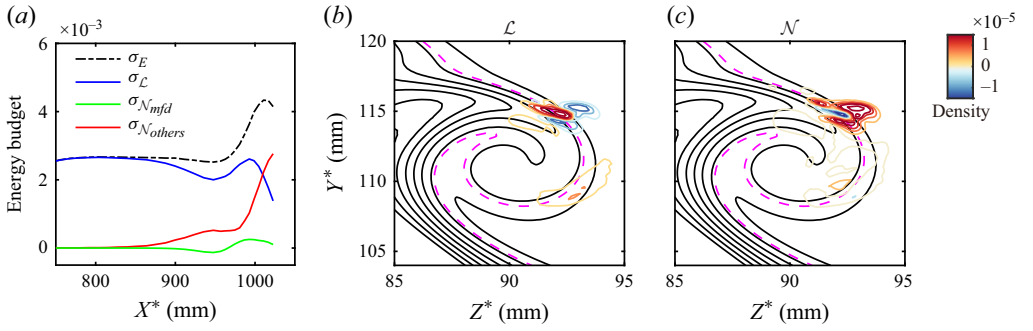


Figure 10. Decomposition of the subharmonic disturbance energy budget for case B1. The density of the linear and nonlinear energy budget at $X^* = 1007$ mm are shown in panels (*b*) and (*c*), where the pink dashed lines represent the critical layer.

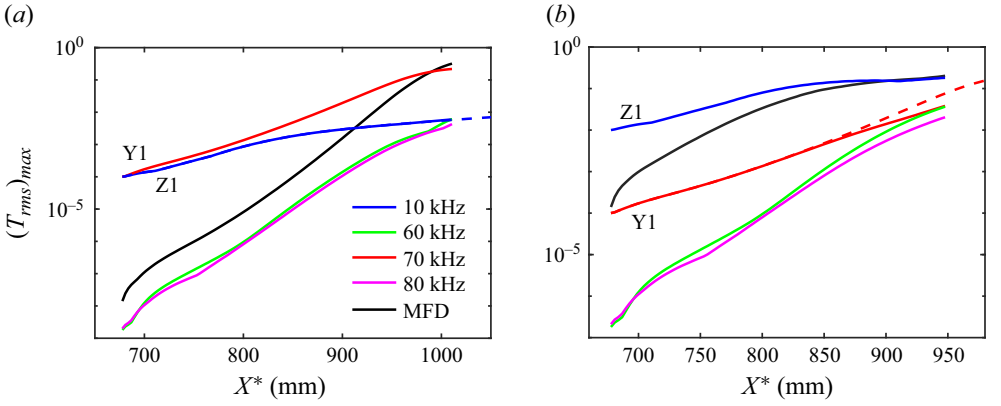


Figure 11. Variations in the maximum temperature disturbance along the streamwise direction of the Z1–Y1 mode interaction dominated by the (*a*) Y1 mode (case C1) and (*b*) Z1 mode (case C2), where the dashed lines represent the results of the self-interaction case.

mode is primarily attributed to nonlinear interactions with the primary mode, where the contribution from MFD appears to be relatively insignificant. This energy redistribution mechanism fundamentally differs from previous studies on parametric resonance, where saturated primary modes catalyse secondary instability growth (Wu, Stewart & Cowley 2007; Chen *et al.* 2017). Figures 10(*b*) and 10(*c*) map the energy budget near the synchronisation location ($X^* = 1007$ mm), showing that $\sigma_{\mathcal{L}}$ and $\sigma_{\mathcal{N}}$ exhibit spatially anti-correlated distributions: regions of positive linear contribution density correspond spatially to negative nonlinear contribution density.

4.3. *Detuned interactions*

An intriguing detuned interaction occurs between a high-frequency Y1 mode and a low-frequency Z1 mode. Such interactions may drive multi-scale turbulence generation due to pronounced spatio-temporal disparities between modal frequency spectra and spatial structures. To probe this mechanism, we examine the representative Y1 (70 kHz, outer) and Z1 (10 kHz, inner) mode interaction, as shown in figure 11. Specifically, two scenarios were considered by selectively prescribing the dominant mode. When the Y1

https://doi.org/10.1017/jfm.2026.11620 Published online by Cambridge University Press

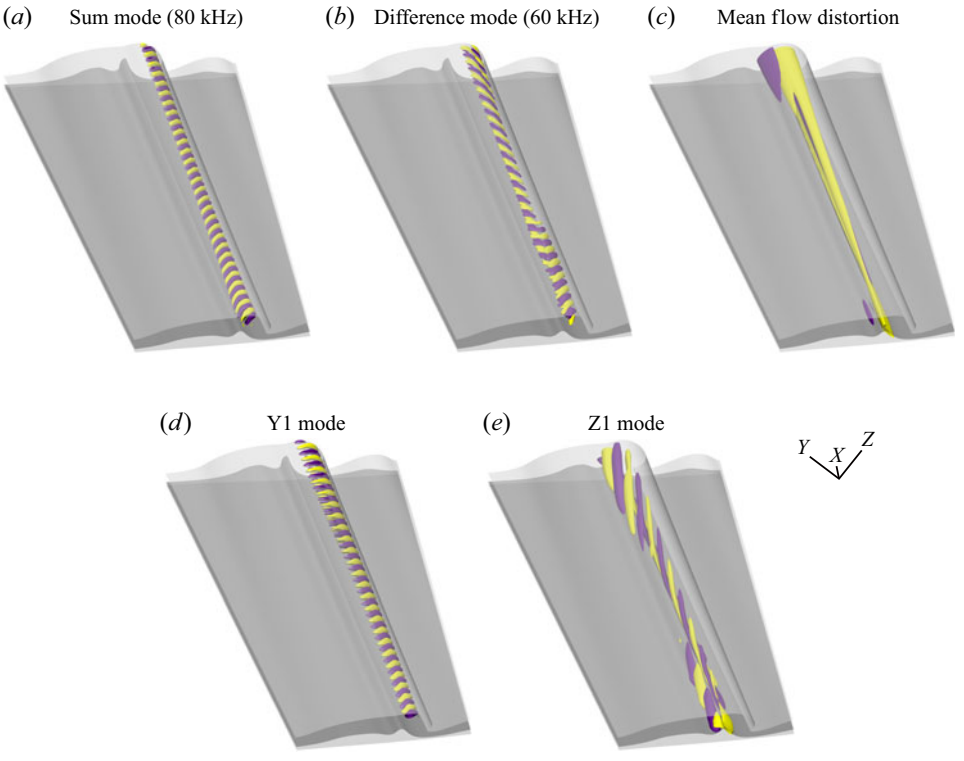


Figure 12. Evolution process of streamwise velocity perturbations of the (*a*) difference mode, (*b*) sum mode, (*c*) MFD, (*d*) Y1 mode and (*e*) Z1 mode under the Z1 mode dominant condition. The shape functions are normalised at each streamwise station. The yellow isosurface and the purple isosurface represent negative and positive velocity disturbance at 0.5.

mode dominates (figure 11*a*), the Z1 mode evolves similarly to its self-interaction case, suggesting minimal cross-impact before the calculation fails to converge. Conversely, when the Z1 mode dominates (figure 11*b*), the growth rate of the Y-mode is reduced.

Figure 12 illustrates the evolution of the streamwise velocity disturbance shape function under the dominant influence of the Z1 mode. Throughout the streamwise evolution, the distribution of both the Y1 mode (figure 12*d*) and Z1 mode (figure 12*e*) remain nearly unchanged and can be distinctly identified by two separate base velocity isosurfaces. For both difference and sum modes, their shape functions concentrate near the critical layer of the Y1 mode. It can be observed that the MFD gradually shifts from the root region of the streamwise vortex towards the shoulder region, which will predictably lead to nonlinear interactions with the Y-mode located at the shoulder. Subsequent analysis (§ 4.4) will show that the MFD plays a dominant role in suppressing the Y1 mode.

4.4. *Role of MFD*

Prior analyses of nonlinear streamwise vortex interactions reveal that MFD plays a pivotal role in disturbance saturation. As demonstrated in figure 8, MFD drives disturbances towards uniform saturation amplitudes across all frequencies during nonlinear evolution and concurrently shifts the spectral peak (linear regime) to a lower frequency band. To elucidate this critical mechanism, the present section investigates how MFD reconstructs the base flow shear distribution and subsequently modulates modal disturbance evolution.

https://doi.org/10.1017/jfm.2026.11620 Published online by Cambridge University Press

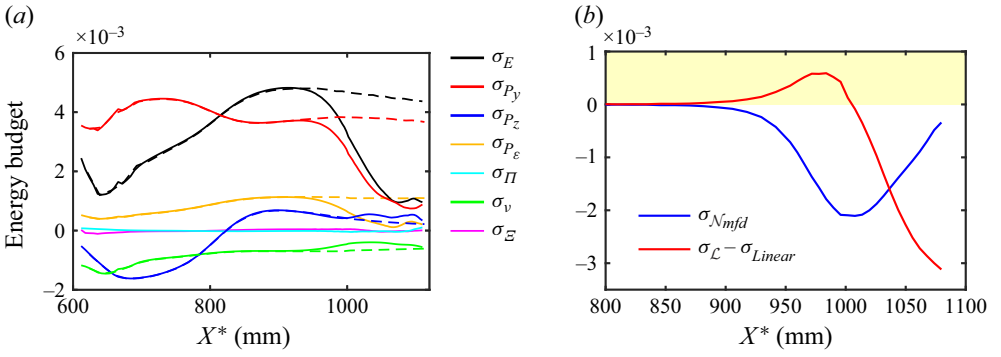


Figure 13. (*a*) Energy budget of the most unstable Y1 mode at 70 kHz along the streamwise direction for the linear (dashed lines) and nonlinear (solid lines) cases. (*b*) Direct nonlinear energy transfer from MFD ($\sigma_{\mathcal{N}_{mfd}}$) and linear energy transfer implicitly caused by MFD via modifying the shape function ($\sigma_{\mathcal{L}} - \sigma_{Linear}$) to the Y1 mode.

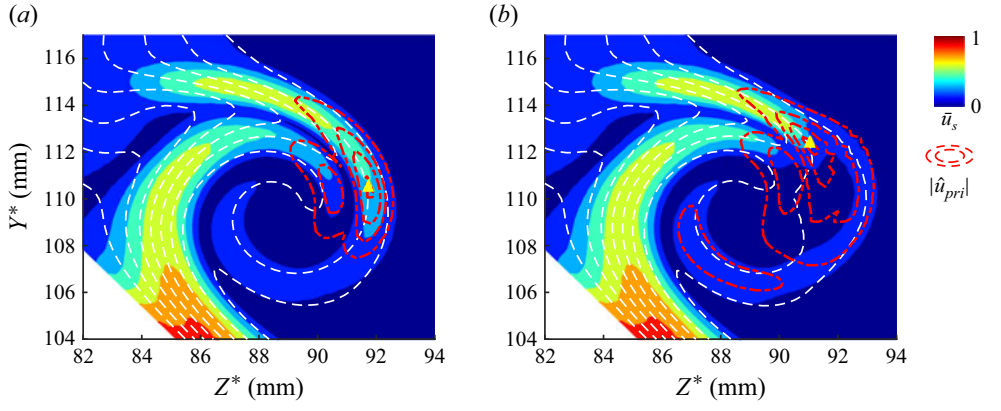


Figure 14. Comparison of the base flow and the shape function of the primary mode at 70 kHz at $X^* = 1000$ mm in the (*a*) linear and (*b*) nonlinear cases. The white dashed lines denote the non-dimensional base flow $\bar{u} = 0.1 : 0.1 : 0.8$. The coloured contour is referred to as the shear magnitude of the streamwise velocity $\bar{u}_s$. The red dashed contour denotes the streamwise velocity magnitude, namely $|\hat{u}|$, of the primary disturbance.

4.4.1. *Energy transfer analysis*

Figure 13(*a*) shows the streamwise evolution of the energy budget for the 70 kHz Y1 mode in the self-interaction case A1. As expected, wall-normal production (P_y) dominates throughout. The MFD significantly modifies production terms through dual mechanisms: direct nonlinear energy transfer ($\sigma_{\mathcal{N}_{mfd}}$) and indirect shape function modification ($\sigma_{\mathcal{L}} - \sigma_{Linear}$). The former always exerts a damping effect, while the latter initially enhance the energy transfer from the base flow and then eventually causes the disturbance to lose energy, as displayed in figure 13(*b*). Similar energy characteristics also occur in Z1 modes. Figure 14 unveils how MFD affects the disturbance by distorting the vortex profile. The shear magnitude of the streamwise velocity $\bar{u}_s$ (Zhang *et al.* 2022) is defined as

$$\bar{u}_s = \left[\left(\partial(\bar{u} + u_{mfd})/\partial Z\right)^2 + \left(\partial(\bar{u} + u_{mfd})/\partial Y\right)^2\right]^{1/2}. \tag{4.1}$$

https://doi.org/10.1017/jfm.2026.11620 Published online by Cambridge University Press

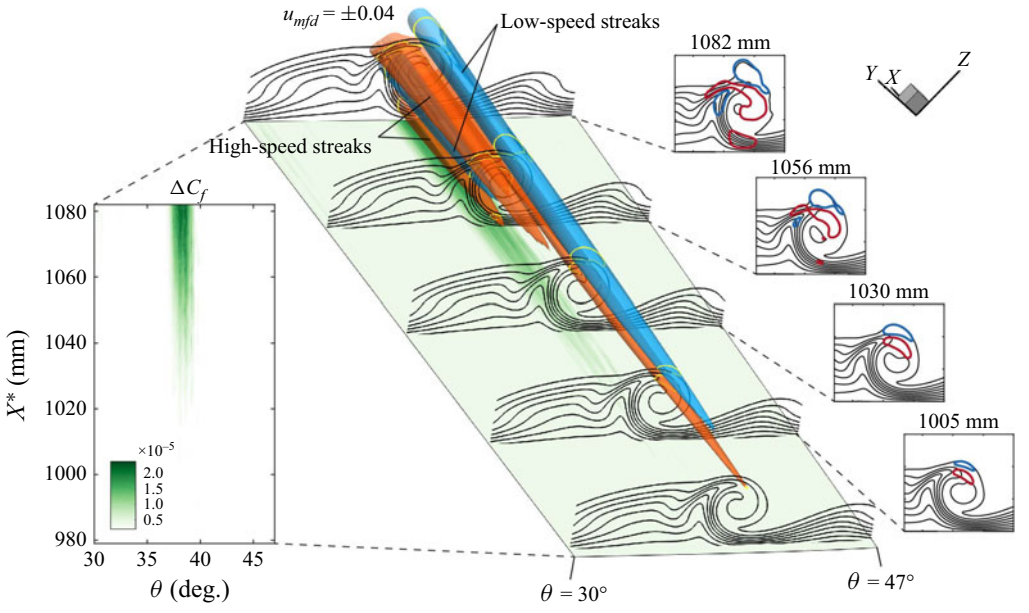


Figure 15. MFD structure generated by the 70 kHz Y1 mode is presented, along with profiles at four stations. In these profiles, red and blue denote the high-speed and low-speed streaks, respectively. The increase in the wall friction coefficient caused by MFD is also illustrated.

The MFD eliminates the high-shear layer at the vortex shoulder where the linearly unstable primary mode resides, thereby forcing the shape function to diffuse upward.

Figure 15 presents the spatial structure of the MFD and the corresponding modifications in the skin friction coefficient relative to the base flow. The MFD consists of high- and low-speed streaks (HSS and LSS) near the high-shear layers of the base flow. Before $X^* = 980$ mm, the HSS and LSS are constricted side by side atop of the streamwise vortex. Simultaneously, the distortion's shape function starts to expand, locally reducing the shear strength of the base flow, as shown in figure 14. Subsequently, the LSS stretches to the vortex's top, creating a substantial low-speed region. Finally, at $X^* = 1082$ mm, the HSS expands towards the wall, increasing the friction coefficient.

For case C1, the Y1 mode was significantly less amplified during the Z1 mode's saturation phase. To determine the underlying mechanism, we conducted an energy transfer analysis (figure 16*a*), which reveals that MFD dominates energy redistribution over other nonlinear interactions. Specifically, the spatial distribution of the MFD energy budget density at $X^* = 935$ mm (figure 16*b*) shows that although the Y1 mode amplitude remains sub-saturated, MFD shifts to the streamwise vortex shoulder, directly overlapping the Y1 mode's region. The high- and low-speed streaks on the vortex shoulder exhibit distribution patterns similar to the self-interaction Y1 mode case.

4.4.2. *Sensitivity analysis*

In the preceding analysis, the MFD significantly influences the energy budget of disturbances, driving nonlinear outcomes that deviate markedly from linear predictions. Notably, the dominant mode in the nonlinear analysis shifts to a lower frequency. This motivates our exploration of the influence of MFD on mode evolution and interaction. To the best of the authors' knowledge, this is the first study that addresses the sensitivity of streamwise vortex modes.

https://doi.org/10.1017/jfm.2026.11620 Published online by Cambridge University Press

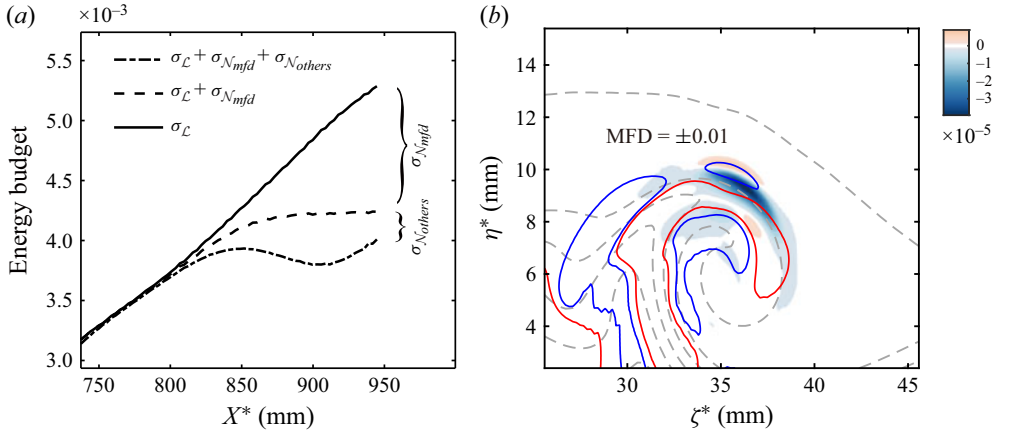


Figure 16. (*a*) Energy budget of the 70 kHz disturbance in the case dominated by the Z1 mode (case C2). (*b*) Energy budget density owing to the MFD at $X^* = 935$ mm. Here, the red and blue contour lines indicate values of $+0.01$ and -0.01, respectively.

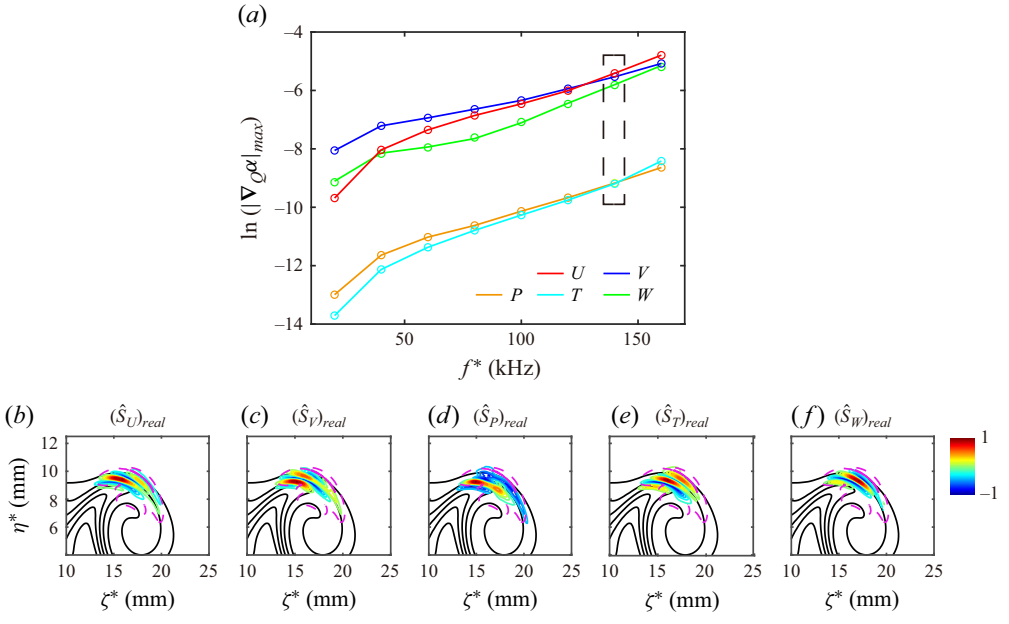


Figure 17. (*a*) Maxima amplitude of the Y1 mode sensitivity profile to base distortion, namely $\nabla_Q \alpha$, at $X^* = 960$ mm. (*b–f*) Real parts of the density of the sensitivity profile at 120 kHz. The pink dashed line indicates 99 % of the perturbation energy as defined by (2.5), serving as the reference for the modal distribution.

Figure 17 displays the frequency-dependent sensitivity amplitude of the Y1 mode to different base flow components. Given the small streamwise variation in sensitivity, results are shown exclusively at a representative station $X^* = 960$ mm. It reveals that all sensitivity components increase rapidly with frequency, demonstrating that higher-frequency modes are more sensitive to base flow distortion – a finding consistent with enhanced MFD effects at higher frequencies (see reduced peak frequency in figure 8). Notably, velocity-component sensitivities exceed temperature/pressure sensitivities by orders of magnitude,

https://doi.org/10.1017/jfm.2026.11620 Published online by Cambridge University Press

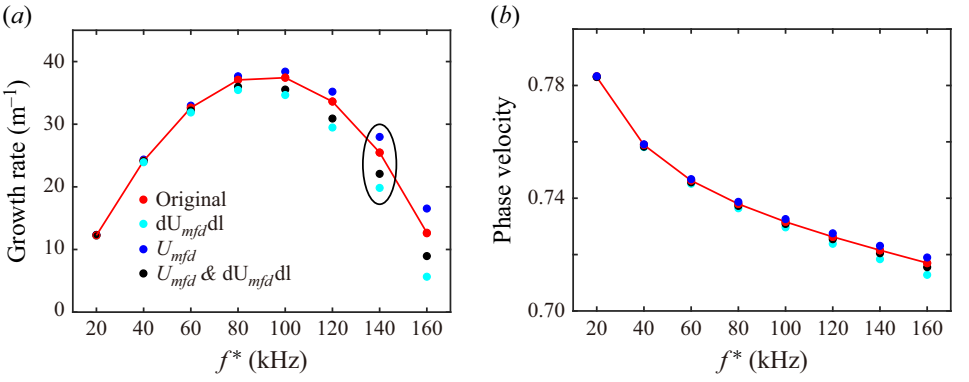


Figure 18. (*a*) Modified modal growth rate and (*b*) modified phase velocity at $X^* = 960$ mm under the distortion of streamwise base velocity δU. The distortion profile is abstracted from the baseline case (refer to figure 15). Red dots denote the growth rate of the original mode, blue dots illustrate the effect of the distortion itself, blue dots indicate the contribution from the change in base-flow shear and the black dots represent their combined effect.

indicating that base velocity distortions dominate stability modifications. This velocity-dominant trend aligns with observations from Park & Zaki (2019) for a flat-plate boundary layer. Furthermore, normalised sensitivity density distributions at one representative frequency (140 kHz), coinciding with the mode shape region, concentrate exclusively on the wall-normal high-shear layer, highlighting the important role of the latter. Since the streamwise velocity component are substantially stronger than other velocity components in MFD, subsequent analysis focuses solely on its impact on modal stability.

The MFD's influence is quantified by multiplying its profile with the sensitivity function. Both the streamwise velocity (U) and its spatial derivatives ($\partial U/\partial l$) were evaluated using distortion profiles from the baseline case (figure 15). Interestingly, these components exhibit opposing effects: while modification of base flow derivatives ($\partial U_{mfd}/\partial l$) weaken modal growth as well as the phase velocity, the base flow velocity distortion (U_{mfd}) itself strengthens them, with the former being dominant, as shown in figure 18.

Following the work of Park & Zaki (2019), we further decompose the sensitivity to the streamwise velocity into four components, specifically $\hat{\boldsymbol{S}}_U = \hat{\boldsymbol{S}}_U^1 + \hat{\boldsymbol{S}}_U^2 + \hat{\boldsymbol{S}}_U^3 + \hat{\boldsymbol{S}}_U^4$, which correspond to the shear of the streamwise velocity, the convective term of the flow, the dissipation caused by viscosity, and the remaining terms associated with temperature and pressure, respectively. The forms of these components are given in Appendix A.

Figure 19 illustrates the spatial distribution characteristics of the streamwise velocity sensitivity at the $X^* = 960$ mm station. It is evident that the shape functions exhibit a typical wave packet structure in the η–ζ plane. The real and imaginary parts display a phase difference of approximately $\pi/2$. As shown in panels (*e–h*), all the components exhibit a multi-pole distribution near the critical layer. The spatial distribution of the real part of the sensitivity reflects the characteristics of the modal phase velocity sensitivity to the base flow. The sensitivities to velocity shear ($\hat{S}_U^1$) and those associated with temperature and pressure terms ($\hat{S}_U^4$) exhibit remarkably similar structures: both display positive values above and negative values below in the vicinity of the critical layer. Sensitivity distributions related to convective terms and viscous terms ($\hat{S}_U^2$, $\hat{S}_U^3$) are

https://doi.org/10.1017/jfm.2026.11620 Published online by Cambridge University Press

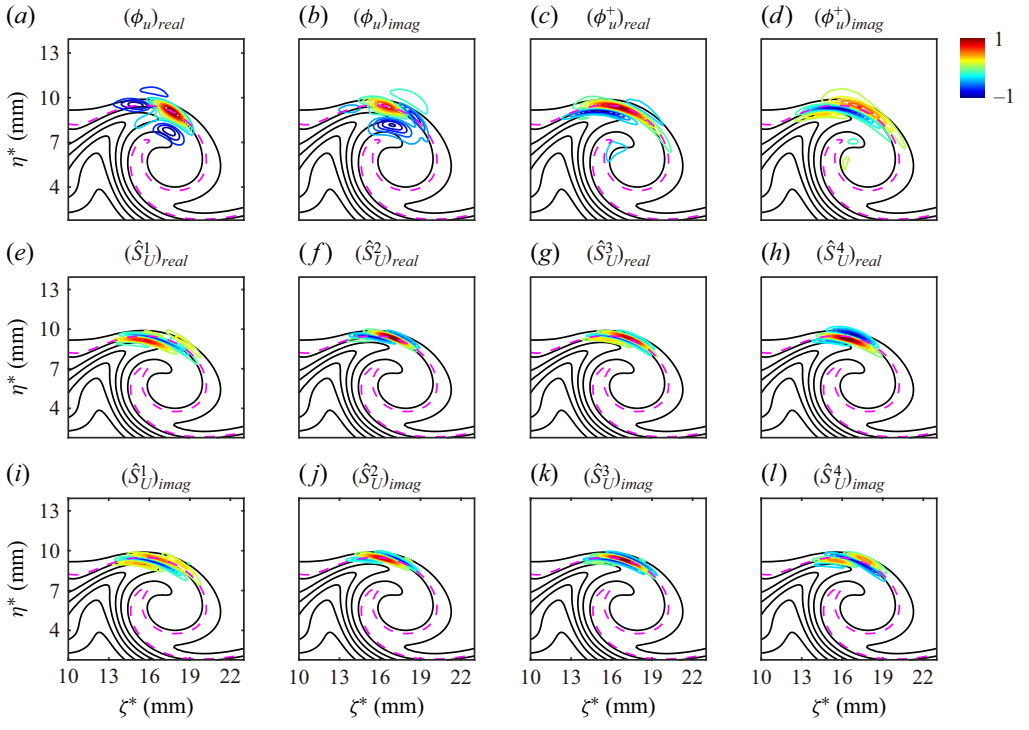


Figure 19. Spatial distribution of the streamwise velocity sensitivity at $X^* = 960$ mm, showing the real and imaginary parts of the streamwise velocity component for the (*a*,*b*) direct mode and (*c*,*d*) adjoint mode, as indicated by the circle in figure 18. The real and imaginary parts of the density of the streamwise velocity sensitivity are respectively illustrated in panels (*e–h*) and (*i–l*).

predominantly positive near the critical layer. The imaginary part of the sensitivity directly reflects the negative variation in the modal growth rate, exhibiting a positive–negative distribution around the critical layer.

Figure 20 compares the contribution of the different sensitivity components to the variations of the growth rate and phase velocity at the same place. As depicted in figure 20(*a*), the bar chart for the growth rate contribution ($-\alpha_i$) reveals that the shear of the base flow field $\hat{\mathcal{S}}_U^1$ predominantly governs the influence of MFD on modal stability, followed by the convective component $\hat{\mathcal{S}}_U^2$, and the temperature and pressure component $\hat{\mathcal{S}}_U^4$. While $\hat{\mathcal{S}}_U^1$ and $\hat{\mathcal{S}}_U^4$ show a stabilising effect, $\hat{\mathcal{S}}_U^2$ exhibits a destabilising effect. The viscous component $\hat{\mathcal{S}}_U^3$ exhibits negligible impact on the mode. For the phase velocity in figure 20(*b*), the streamwise velocity shear component $\hat{\mathcal{S}}_U^1$ constitutes the primary positive contribution, whereas the convection and temperature-pressure terms $\hat{\mathcal{S}}_U^2$ and $\hat{\mathcal{S}}_U^4$ both display negative effects, and the contribution value of the viscous component $\hat{\mathcal{S}}_U^3$ remains nearly zero. In conclusion, modal instability is most sensitive to the change of the base flow shear. It is worth noting that although MFD generated during the evolution of modal disturbances varies slightly depending on the frequency, for modes belonging to the same branch, the results are qualitatively consistent.

https://doi.org/10.1017/jfm.2026.11620 Published online by Cambridge University Press

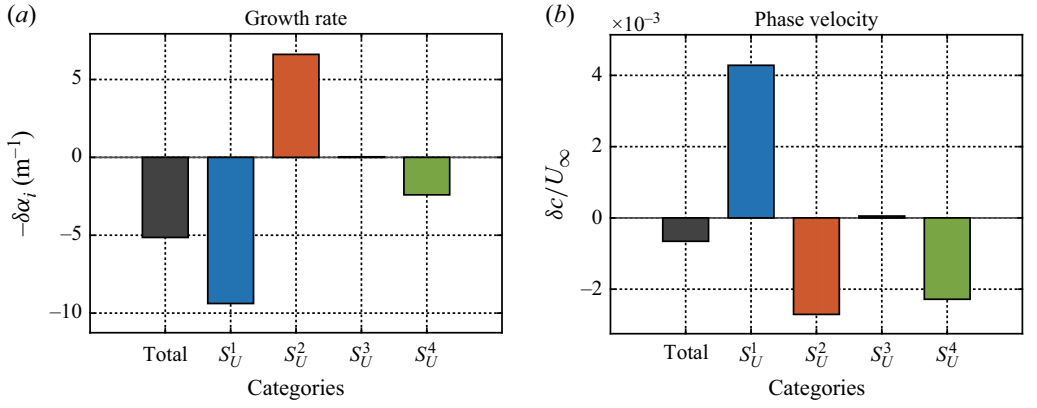


Figure 20. Histogram of the (*a*) growth rate and (*b*) phase velocity distortions of the Y1 mode at $X^* = 960$ mm, which is illustrated by the circle in figure 18, when the flow is distorted by U_{mfd} in the baseline case. The black columns represent the total distortion $\delta\alpha_i$ and δc_{ref} in panels (*a*) and (*b*), respectively. Each total distortion is divided into four parts.

5. Vortex breakdown simulations

The NPSE3D method demonstrates its capability to effectively capture the characteristics of streamwise vortex mode development in the early stages of disturbance evolution. However, as nonlinear interactions become increasingly significant in the later stages, substantial changes in the streamwise wavenumber and disturbance shape function arise, violating the assumption inherent to the parabolised formulation. To resolve this limitation and also verify the computational results of the NPSE3D, we perform DNS to analyse the breakdown mechanisms of shoulder vortices in the late transition stage. To achieve high-fidelity results while optimising computational resources, the mesh is significantly refined in the azimuthal angle range $\theta = 45°$–$60°$ ($\Delta\theta = 0.10°$), where the shoulder streamwise vortex resides. The grid for simulating the transition condition is interpolated from the basic flow grid and truncated in the streamwise direction from $X^* = 600$ to 1400 mm, with the sponge zone lying between $X^* = 1300$ and 1400 mm. The grid contains 1980 points in the streamwise direction, 369 points in the lateral direction and 251 points in the wall-normal direction. The grid resolution is $\Delta x^+_{max} \times \Delta y^+_{min} \times \Delta z^+_{max} = 20 \times 0.5 \times 20$. As per the research by Chen *et al.* (2022), the current simulation can be regarded as QDNS (with grid resolution lying between that of large eddy simulation and that of DNS). As shown in Appendix B, Δx^+_{max} and Δz^+_{max} remain consistently around 10 for the region on which we focus ($X^* < 1200$ mm), which is sufficient for our purpose.

At the inlet boundary conditions, modal profiles incorporating each Z1 and Y1 modes or both were imposed, along with random noise constituting 0.01 % of the incoming flow. The impact of these random noise amplitude on the modal evolution process was evaluated and found to be negligible. The numerical simulation parameters are listed in table 3.

Figure 21 compares Q-criterion isosurfaces from DNS, NPSE3D and LPSE3D simulations during transition onset (case D1). The results demonstrate that NPSE3D successfully reproduces the key features of the DNS flow structures. The stretch of secondary vortex-leg connecting to the primary vortex (as highlighted in figure 21) is reminiscent of the 'finger vortices' reported by Chen *et al.* (2021) during stationary cross-flow breakdown at Mach 6. Specifically, the upstream hairpin vortex splits downstream, presumably due to vortex reconnection (Yao & Hussain 2022) between primary hairpins and MFD-induced streamwise vortices, as sketched by figure 22.

https://doi.org/10.1017/jfm.2026.11620 Published online by Cambridge University Press

Case	Inlet condition ($\lvert\hat{T}\rvert_{max}$)
D1	0.01 % Noise + 0.01 % Y1 (70 kHz)
D2	0.01 % Noise + 1 % Z1 (10 kHz)
D3	0.01 % Noise + 1 % Z1 (10 kHz) + 0.01 % Y1 (70 kHz)

Table 3. Simulation cases.

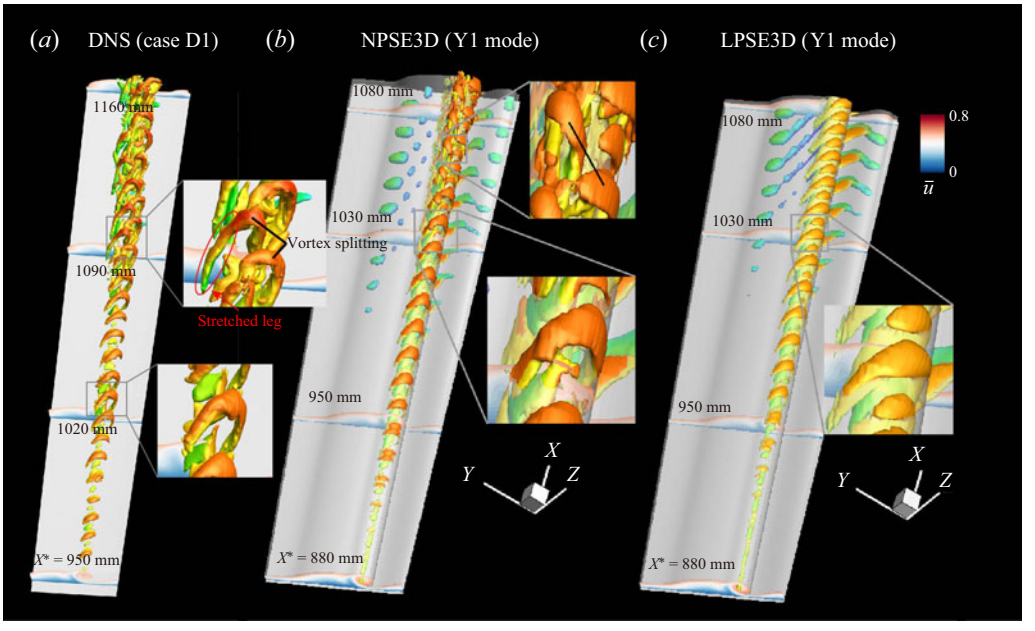


Figure 21. Visualisation of the instantaneous flow field structure using the Q criterion ($Q = 0.0004$ for DNS and 0.0001 for NPSE3D/LPSE3D), with isosurfaces coloured by the time-averaged and base streamwise velocity. Local enlarged views of the vortex structures at selected stations are presented for (*a*) DNS, (*b*) NPSE3D and (*c*) LPSE3D.

Notably, the splitting of such vortex structures has also been observed during the transition process of cross-flow vortices on swept wings and Görtler vortices during their late-stage transition stage (Bonfigli & Kloker 2007; Casacuberta *et al.* 2022; Brockhaus *et al.* 2024), as well as of streaky structures downstream a randomly distributed roughness patch (Wang *et al.* 2024).

Figure 23 illustrates the evolution characteristics of disturbances in case D1 at three representative stations. At the streamwise station of $X^* = 900$ mm, the disturbance remains in its linear growth phase, with the root mean square (rms) distribution featuring Y1 mode distribution. Further downstream at $X^* = 1000$ mm, the MFD amplitude gradually accumulates and significantly influences the local flow profile. Through energy analysis, as detailed in the previous section, it is evident that the MFD primarily modulates the growth of the modal disturbance by diminishing the dominant source term associated with the local velocity gradient, thereby inducing a saturation state for the perturbation. Meanwhile, the disturbance progressively expands to encompass the entire wall-normal shear layer region with its peak moving towards the upper left corner of the shear layer. This observation qualitatively aligns with the NPSE3D

https://doi.org/10.1017/jfm.2026.11620 Published online by Cambridge University Press

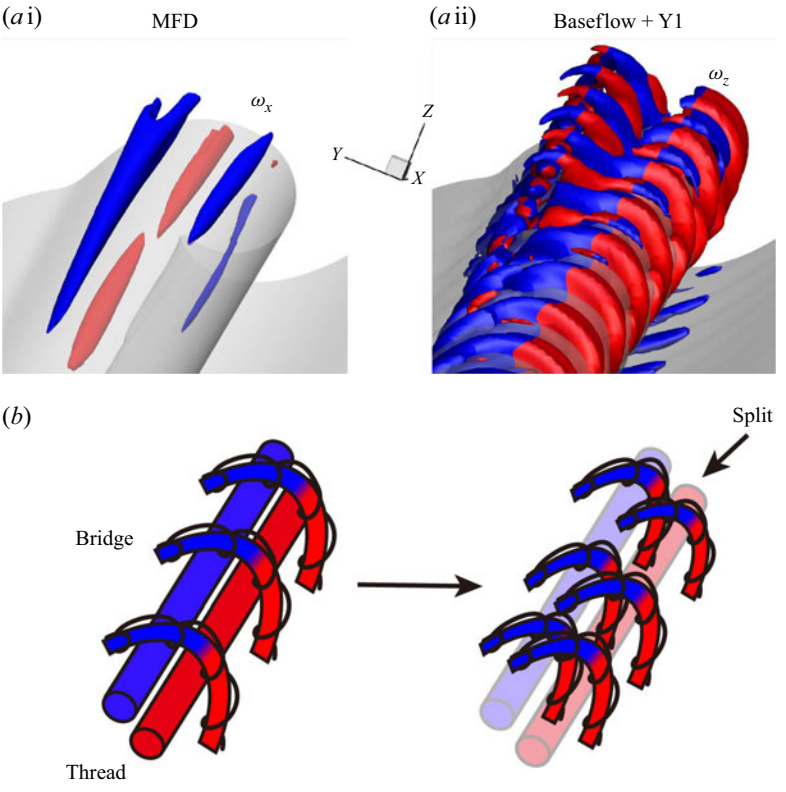


Figure 22. (*a*) Schematic vortex topology: (*i*) MFD and (*ii*) base flow superimposed with the Y1 mode from NPSE3D. Structures are visualised by the $Q = 0.0005$ isosurface coloured by streamwise vorticity (red, positive; blue, negative). (*b*) Cartoon of the splitting process: the MFD and primary mode can be viewed as thread and bridge, respectively.

results simulating the self-interaction of a single Y1 mode (refers to figure 14). Further downstream to $X^* = 1100$ mm, as the flow field undergoes deformation, the disturbance evolution enters the downwash region associated with the streamwise vortex. A significant peak emerges in this region, displaying morphological similarities to the instability process of cross-flow vortices at their downwash region (Xu *et al.* 2019). However, no comparable unstable mode characteristics are identified in the multi-dimensional stability analysis of the upstream streamwise vortex, suggesting that this disturbance arises from nonlinear interactions rather than inherent linear mechanisms. Figure 23(*d*) compares the perturbation amplitudes from DNS and NPSE3D, showing a good agreement between the two approaches.

To achieve a better comprehension of the transition process, figure 24 illustrates several critical features of the flow field during the late saturation stage of the disturbance. These include the visualisation of vortex structures using the Q criterion, the spatial distribution of the instantaneous wall friction coefficient and the rise of the mean flow wall friction coefficient relative to the base flow. Notably, the spatial evolution of the MFD is very reminiscent of the NPSE3D results (refer to figure 15). Upon reaching the saturation stage, the Y1 mode induces a typical hairpin vortex structure in the shoulder region of the streamwise vortex. As the flow evolves downstream, these vortex structures migrate towards the wall along the downwash region of the vortex. The square-marked regions in the figure highlight specific locations where the wall friction coefficient increases,

https://doi.org/10.1017/jfm.2026.11620 Published online by Cambridge University Press

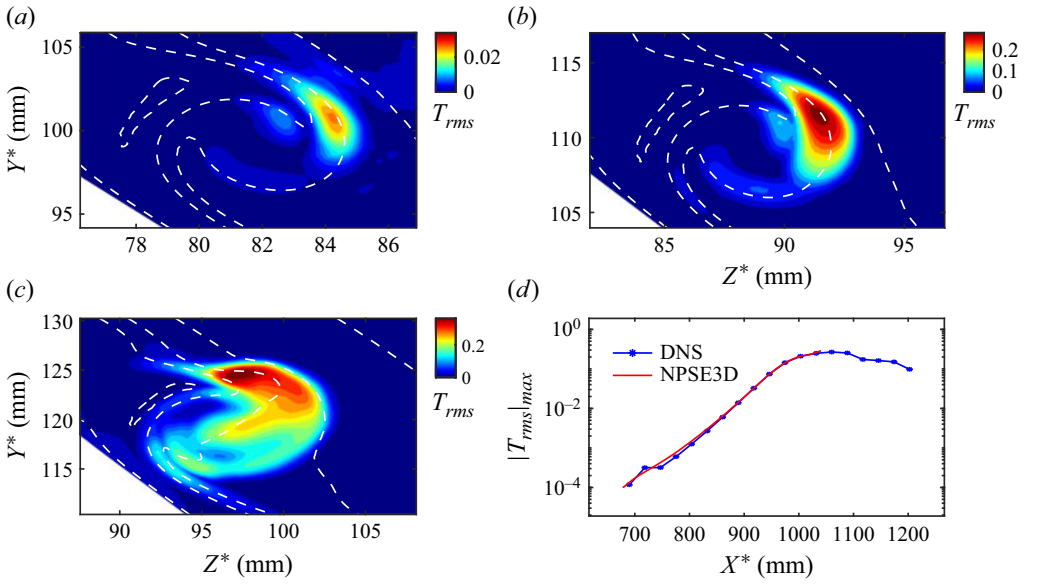


Figure 23. Spatial distribution of the root mean square (rms) of temperature fluctuations of case D1 at $X^* =$ (*a*) 900 mm, (*b*) 1000 mm and (*c*) 1100 mm, as obtained from DNS. The amplitude of disturbance at 70 kHz in DNS is compared with NPSE3D in panel (*d*).

with the vorticity distribution in the Z-direction (depicted by red for clockwise rotation and blue for counterclockwise rotation) offering a more intuitive visualisation of the vortex dynamics. When the shape function of the Y1 mode fully encompasses the shoulder region of the streamwise vortex, it gradually transforms from a hairpin to a horseshoe configuration. During this transformation, the right leg of the horseshoe vortex generates a counter-rotating vortex roll near the wall, significantly influencing the local wall friction coefficient. Simultaneously, the disturbance near the wall triggers an HSS, ultimately leading to adjustments in the shear layer within the streamwise vortex and resulting in an increase of the time-averaged wall friction. As the horseshoe vortex evolves downstream, its right leg is stretched due to wall drag, eventually forming a streamwise-extended structure. Concurrently, the roll atop the horseshoe vortex breaks down under the influence of the MFD, cascading into a series of vortex clusters. This process catalyses the breakdown of the streamwise vortex.

Figure 25(*a*) reveals wall friction evolution at $\theta = 53°$ for cases D1–D3, showing that transition onset (marked by friction rise) aligns temporally regardless of the dominant mode. During late transition stages (figure 25*b–d*), all cases exhibit friction overshoot – notably, Z1 mode induces earlier overshoot due to their proximity to the wall, where MFD directly modifies near-wall profiles. Additionally, the mode-interaction case (D3) exhibits an advanced overshoot location compared with Y1 or Z1 mode-only cases. This acceleration mechanism is corroborated by the Q-criterion at friction-rise onset ($X^* \approx 1050$ mm, refer to figure 26). While Z1 mode generates persistent near-wall large-scale structures, mode interactions dissipate these features rapidly. Collectively, these findings demonstrate that modal interactions accelerate disturbance saturation and structural breakdown, thereby hastening transition. Moreover, the friction coefficient peak in interaction cases exceeds single-mode cases, presumably due to MFD amplification through multi-modal interactions.

https://doi.org/10.1017/jfm.2026.11620 Published online by Cambridge University Press

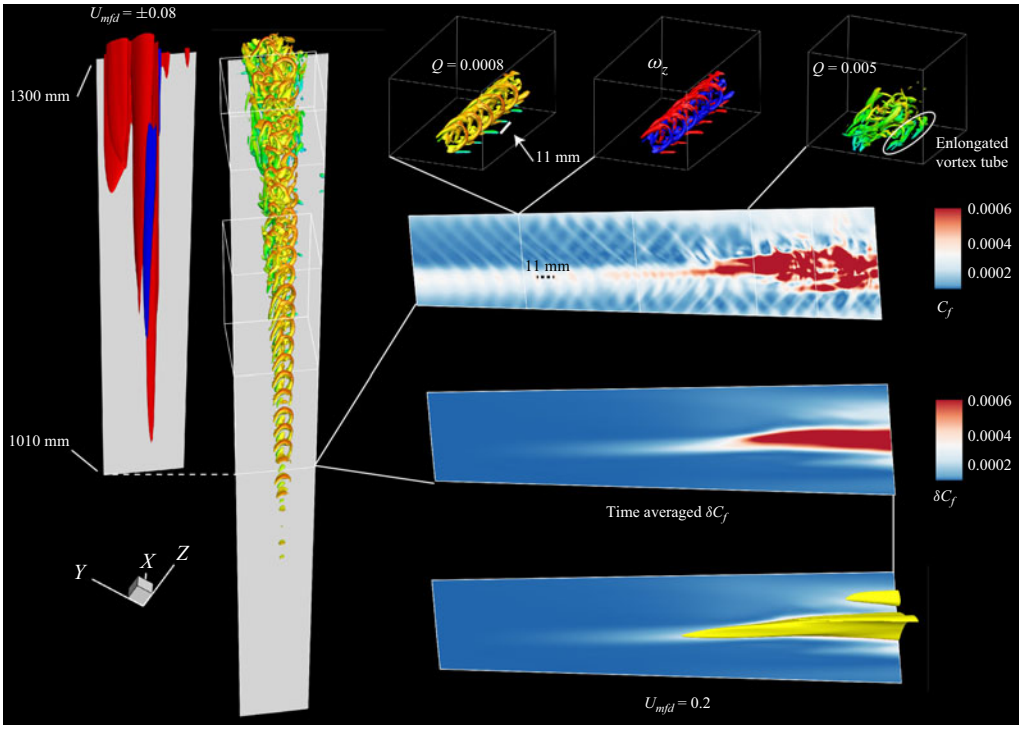


Figure 24. MFD, flow field visualised via Q-criterion ($Q = 0.0004$), wall friction of the instantaneous flow field and the time-averaged wall friction elevated relative to the base flow for the Y1 mode case at the late stage. Additionally, the flow field marked by rectangular boxes is included to illustrate the vortex structures associated with wall friction lift-up, coloured by streamwise velocity and vorticity in the Z-direction, as well as the vortex structures in the flow field at a later stage.

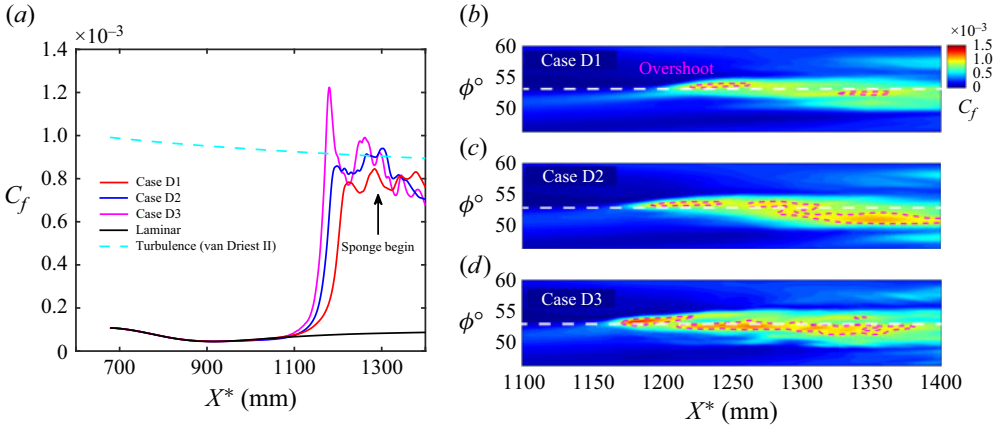


Figure 25. (*a*) Results of wall friction rise at $\theta° = 53°$, which is illustrated in panels (*b–d*) as the white dashed line, for the Y1 mode (red solid line), Z1 mode (blue solid line) and interaction case (black solid line), together with the laminar state and the turbulence estimate (van Driest 1951) as a reference. (*b–d*) Time-averaged wall friction in the three cases, where the purple dashed contour lines indicate overshoot areas.

https://doi.org/10.1017/jfm.2026.11620 Published online by Cambridge University Press

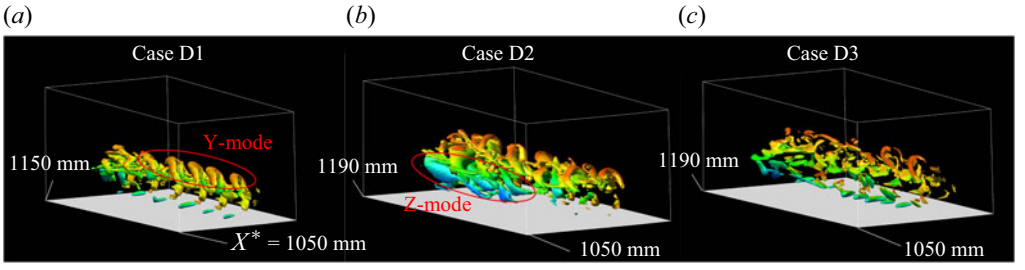


Figure 26. Flow field structures at the wall friction lift-up positions for the (*a*) Y1 mode dominant (case D1), (*b*) Z1 mode dominant (case D2) and (*c*) interaction (case D3) cases at $Q = 0.0004$.

Finally, we examine the disturbance spectra within the near-wall region to elucidate the transition mechanisms. Figure 27 depicts the spatial distribution of temperature disturbances in the streamwise and frequency domains for the three cases. For the Y1 mode case, the dominant frequency of 70 kHz and its first harmonic (140 kHz) are distinguishable. Furthermore, during the initial stages of transition at approximately $X^* = 1050$ mm, a broad peak centred around 35 kHz is observed. This finding aligns with subharmonic growth documented in § 4.2, suggesting that subharmonic instability mechanisms also play a significant role. For the Z1 mode case, disturbances exhibit substantial amplitudes in the upstream region, resulting in a faster growth rate of low-frequency components compared with the Y1 mode scenario. Additionally, the prominence of disturbance peaks within the 60–100 kHz frequency range underscores the notable contribution of Y1 mode instabilities during Z1 mode dominant transitions. In the interaction case, the spectral features become more complex, showing the coexistence of both Z1 and Y1 modes, their harmonics, as well as difference and sum frequencies generated by their interactions. Furthermore, higher-order harmonics are excited through interactions between these modes. As previously demonstrated through energy analysis, disturbances primarily extract energy from the shear in the flow field. The nonlinear effects accelerate the process of energy extraction by disturbances from the base flow, thereby enhancing the magnitude of overshoot.

6. Conclusions

This study investigates the nonlinear stability and transition mechanisms of streamwise vortices over the HyTRV lifting body by employing both linear and nonlinear multi-dimensional stability analysis methods (BiGlobal, LPSE3D, NPSE3D) alongside direct numerical simulation (DNS). Linear modal analysis identifies two primary instabilities: the Y-mode located at the vortex top, which exhibits broader frequency ranges, higher amplification rates and higher phase velocities compared with the Z-mode situated at the vortex root. Energy budget decomposition reveals distinct energy production, with Y-modes predominantly sustained by wall-normal shear production (P_y) and Z-mode mostly depending on lateral shear production (P_z). While the cross-flow vortices and Görtler vortices arise from primary instabilities of the boundary layer, the streamwise vortices in the present study are the base flow itself and emerge from the convergence of the fluid. Therefore, the primary instabilities of the streamwise vortices in the present study are analogous to the secondary instabilities of the cross-flow and Görtler vortices.

The nonlinear self-interactions of the Y-mode yield amplitude saturation without triggering the fundamental resonance, in stark contrast with the attachment-line boundary layer where the primary mode is prone to strong fundamental resonance (Chen *et al.*

https://doi.org/10.1017/jfm.2026.11620 Published online by Cambridge University Press

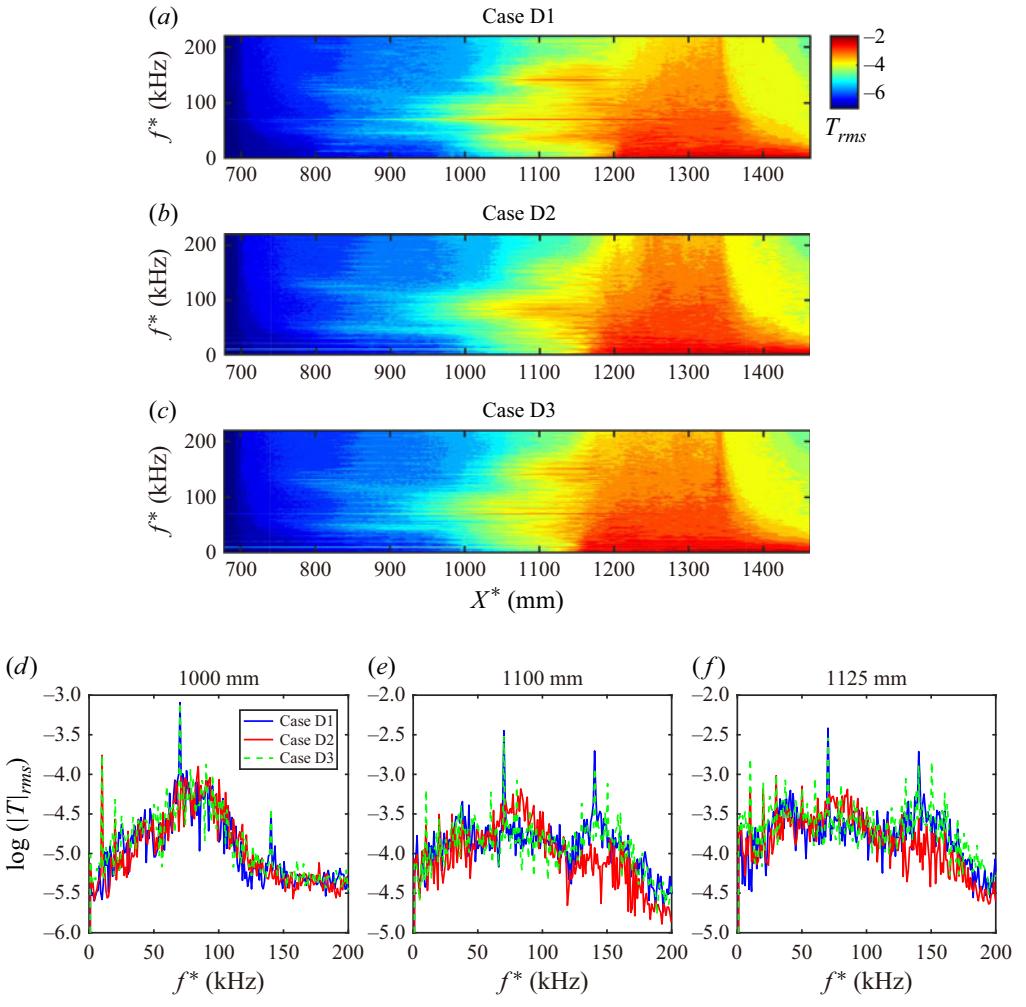


Figure 27. Near-wall disturbance spectra for cases with (*a*) Y1 mode dominant (case D1), (*b*) Z1 mode dominant (case D2) and (*c*) mode interaction (case D3). Comparative results of the disturbance spectra for the three cases at streamwise locations of (*d*) $X^* = 1000$ mm, (*e*) $X^* = 1100$ mm and (*f*) $X^* = 1125$ mm.

2023). Detuned interaction between high-frequency Y-mode and low-frequency Z-mode is also found to be weak in the weakly nonlinear stage. By comparison, moderately strong subharmonic resonance is observed.

Mean flow distortion (MFD) plays a pivotal role in nonlinear development of vortex modes. It weakens the shear layer notably, thereby causing the saturation of the primary mode. Moreover, MFD manifests as longitudinal vortical structures with alternating positive and negative streamwise vortices, which can interact with the primary mode exhibiting a hairpin vortex. By vortex reconnection, the primary hairpin vortex splits into two hairpin vortices. This splitting process continues, resulting in hairpin wave-packet.

Sensitivity analysis further demonstrates that velocity components within base-flow distortions exert the strongest influence on stability modifications, with orders-of-magnitude higher sensitivity than temperature/pressure variations. Higher-frequency modes exhibit significantly greater susceptibility to these sensitivity effects.

https://doi.org/10.1017/jfm.2026.11620 Published online by Cambridge University Press

DNS results are in good agreement with NPSE3D results up to the weakly nonlinear stage, and show details about the breakdowns process during which subharmonic disturbances emerge and become pronounced. Seeding both the Y-mode and the Z-mode turns out to precipitate the transition process.

Although only a specific configuration is considered, the nonlinear stability analyses developed in this work can be straightforwardly applied to other flows featuring streamwise vortical structures. The close similarity regarding the development of vortical structures during the breakdown process in apparently different flows (e.g. Casacuberta *et al.* 2022; Wang *et al.* 2024) implies the universal vortex-splitting mechanism which warrants further studies.

Acknowledgements. The authors acknowledge the fruitful suggestions from Dr G. Tu, Dr B. Wan, Dr S. Dong and Dr S. Liu.

Funding. This study is supported by National Natural Science Foundation of China (grant nos. 12372225 and 12272395) and the National Numerical Wind-tunnel Project (NNW).

Declaration of interests. The authors report no conflict of interest.

Appendix A. Detailed expressions of the sensitivity to streamwise velocity

In this section, we present detailed expressions of the sensitivity of the complex streamwise wavenumber to streamwise base-flow velocity distortions, namely $\hat{S}_U = \hat{S}_U^1 + \hat{S}_U^2 + \hat{S}_U^3 + \hat{S}_U^4$, where the overall component is derived based on the BiGlobal stability analysis matrix presented by Chen *et al.* (2022).

The first term originates from the shear components of the base flow in the streamwise velocity, primarily involving the terms $\partial U/\partial y$ and $\partial U/\partial z$,

$$\widehat{S}_U^1 = \frac{\partial \rho \widehat{u}^{\dagger *} \widehat{v}}{\partial y} + \frac{\partial \rho \widehat{u}^{\dagger *} \widehat{w}}{\partial z}. \tag{A1}$$

Note that in this appendix, the superscript * denotes the complex conjugate part and the over-bar of the base-flow quantities has been omitted for simplicity. The second term arises from the non-parallel effects of the perturbations, incorporating the spatial derivatives of the streamwise velocity perturbations with respect to the base flow,

$$\begin{aligned}\widehat{S}_U^2 = \alpha \Big[& -i\rho\left(\widehat{u}^{\dagger *}\widehat{u} + \widehat{v}^{\dagger *}\widehat{v} + \widehat{w}^{\dagger *}\widehat{w}\right) + i\gamma M^2 \widehat{p}^{\dagger *}\widehat{p} - i\,\mathrm{Pr}\,\rho \widehat{T}^{\dagger *}\widehat{T} \Big] \\ & - i\rho \widehat{u}^{\dagger *}\frac{\partial \widehat{u}}{\partial x} + \frac{\rho}{T} U_x \widehat{u}^{\dagger *}\widehat{T} - \frac{\partial\left(\widehat{u}^{\dagger *}\widehat{T}\rho V/T\right)}{\partial y} - \frac{\partial\left(\widehat{u}^{\dagger *}\widehat{T}\rho W/T\right)}{\partial z} \\ & - \rho \widehat{v}^{\dagger *}\widehat{v}_x + \frac{\rho}{T} V_x \widehat{v}^{\dagger *}\widehat{T} + \mathrm{Pr}\,\rho \frac{T_x}{T}\widehat{T}^{\dagger *}\widehat{T} - \mathrm{Pr}\,\rho \widehat{T}^{\dagger *}\widehat{T}_x + \frac{\rho}{T} W_x \widehat{w}^{\dagger *}\widehat{T} - \rho \widehat{w}^{\dagger *}\widehat{w}_x.\end{aligned} \tag{A2}$$

The third term represents a combination of terms directly associated with viscous dissipation,

$$\begin{aligned}\widehat{S}_U^3 = -i\frac{\alpha}{R}\left[\frac{\partial\left(\mu\mu_m \widehat{v}^{\dagger *}\widehat{T}\right)}{\partial y} + \frac{\partial\left(\mu\mu_m \widehat{w}^{\dagger *}\widehat{T}\right)}{\partial z} - 2G\frac{\partial\left(\mu \widehat{T}^{\dagger *}\widehat{v}\right)}{\partial y} - 2G\frac{\partial\left(\mu \widehat{T}^{\dagger *}\widehat{w}\right)}{\partial z}\right] + \\ \frac{1}{R}\left[-\frac{\partial\left(\widehat{u}^{\dagger *}\widehat{T}_y \mu\mu_m\right)}{\partial y} - \frac{\partial\left(\widehat{u}^{\dagger *}\widehat{T}_z \mu\mu_m\right)}{\partial z} + \frac{\partial^2\left(\mu\mu_m \widehat{u}^{\dagger *}\widehat{T}\right)}{\partial y^2} + \frac{\partial^2\left(\mu\mu_m \widehat{u}^{\dagger *}\widehat{T}\right)}{\partial z^2}\right.\end{aligned}$$

https://doi.org/10.1017/jfm.2026.11620 Published online by Cambridge University Press

$$-\frac{\partial\left(\widehat{u}^{\dagger *}\widehat{T}T_y\mu\mu_{mm}\right)}{\partial y}-\frac{\partial\left(\widehat{u}^{\dagger *}\widehat{T}T_z\mu\mu_{mm}\right)}{\partial z}+\frac{\partial\left(\widehat{v}^{\dagger *}\widehat{T}T_x\mu\mu_{mm}l_0\right)}{\partial y}+\frac{\partial\left(\widehat{v}^{\dagger *}\widehat{T}_x\mu\mu_m\right)}{\partial y}$$
$$+2G\frac{\partial\left(\widehat{T}^{\dagger *}\widehat{T}T_x\mu\mu_{mm}U_y\right)}{\partial y}+2G\frac{\partial\left(\widehat{T}^{\dagger *}\widehat{T}T_x\mu\mu_{mm}U_z\right)}{\partial z}+\frac{\partial\left(\mu\mu_{mm}T_x\widehat{w}^{\dagger *}\widehat{T}\right)}{\partial z}$$
$$+\frac{\partial\left(\mu\mu_m\widehat{w}^{\dagger *}\widehat{T}_x\right)}{\partial z}+2G\frac{\partial\left(\mu\widehat{T}^{\dagger *}\widehat{u}_y\right)}{\partial y}+2G\frac{\partial\left(\mu\widehat{T}^{\dagger *}\widehat{u}_z\right)}{\partial z}+2G\frac{\partial\left(\mu\widehat{T}^{\dagger *}\widehat{u}_x\right)}{\partial y}+$$
$$2G\frac{\partial\mu\widehat{T}^{\dagger *}\widehat{w}_x}{\partial z}\Bigg]. \tag{A3}$$

The fourth term consolidates all contributions involving the temperature and pressure perturbation components,

$$\widehat{\boldsymbol{S}}_U^4=\alpha\big[-i\rho\widehat{p}^{\dagger *}\widehat{T}+iG\widehat{T}^{\dagger *}\widehat{p}\big]-\frac{\gamma Ma_\infty^2}{T}U_x\widehat{u}^{\dagger *}\widehat{p}-\gamma Ma_\infty^2\frac{\partial\left(V\widehat{u}^{\dagger *}\widehat{p}/T\right)}{\partial y} \tag{A4}$$
$$-\gamma Ma_\infty^2\frac{\partial\left(W\widehat{u}^{\dagger *}\widehat{p}/T\right)}{\partial z}-\gamma Ma_\infty^2\frac{V_x}{T}\widehat{v}^{\dagger *}\widehat{p}-\gamma Ma_\infty^2\frac{T_x}{T}\widehat{p}^{\dagger *}\widehat{p}+\gamma Ma_\infty^2\widehat{p}^{\dagger *}\widehat{p}_x$$
$$+\left(2\frac{P_0T_x-P_xT}{T^2}\right)\widehat{p}^{\dagger *}\widehat{T}-\rho\widehat{p}^{\dagger *}\widehat{p}_x-\gamma Ma_\infty^2\,\mathrm{Pr}\,\frac{T_x}{T}\widehat{T}^{\dagger *}\widehat{p}+G\widehat{T}^{\dagger *}\widehat{p}_x$$
$$-\gamma Ma_\infty^2\frac{W_x}{T}\widehat{w}^{\dagger *}\widehat{p}.$$

The terms $G=Pr(\gamma-1)Ma_\infty^2$, $\mu_m=(\mathrm{d}\mu/\mathrm{d}T)/\mu$ and $\mu_{mm}=\mathrm{d}^2\mu/\mathrm{d}T^2/\mu$ are abbreviated for brevity.

Appendix B. DNS resolution

Four sets of grids were employed to assess the independence of the baseflow with respect to streamwise, azimuthal and wall-normal resolutions, namely (641 × 741 × 301), (521 × 741 × 301), (521 × 891 × 251) and (521 × 741 × 251, baseline), as shown in figure 28. There are approximately 150 points within the boundary layer in the shoulder vortex region for the baseline grid adopted in the manuscript. Evidently, further increasing the grid points in either the streamwise, the azimuthal or the wall-normal direction compared with the baseline case barely changes the base flow, thereby verifying the grid convergence.

Figure 29 illustrates the distribution of near-wall mesh discretisations accuracy across most of the surface area in the shoulder vortex region. Apart from the loss of resolution due to disturbances evolving near the wall, the dimensionless wall distances $\triangle x^+$ and $\triangle z^+$ are maintained below 10. For the dominant Y1 mode (70 kHz) and its harmonic (140 kHz), approximately 25 and 15 grid points are used per wavelength for resolution, respectively. The spatial resolution of this mesh system is comparable to that of previous study using also QDNS to analyse the vortical structures (Chen *et al.* 2022), thereby satisfying the accuracy requirements for this research.

https://doi.org/10.1017/jfm.2026.11620 Published online by Cambridge University Press

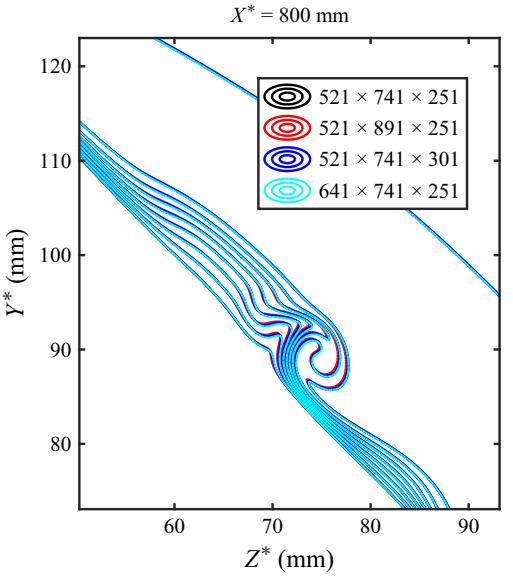


Figure 28. Grid convergence analysis of the baseline flow at $X^* = 800\,\text{mm}$.

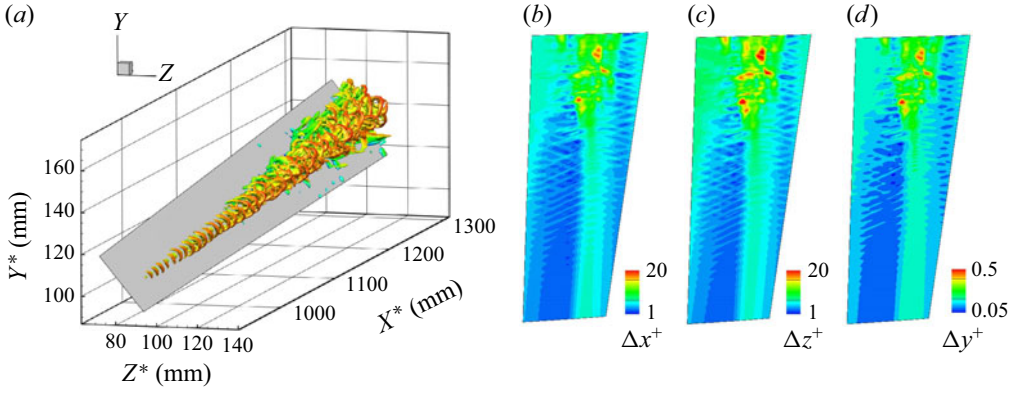


Figure 29. (*a*) Flow field structure in the later stages of the disturbance dominated by the Y1 mode, and (*b–d*) sizing of the mesh in a local wall unit.

References

Araya, D., Bitter, N., Wheaton, B., Kamal, O., Colonius, T., Knutson, A. & Johnson, H. 2025 Linear analysis of boundary-layer instabilities on a finned cone at Mach 6. *AIAA J.* **63** (7), 2594–2614.

Bonfigli, G. & Kloker, M. 2007 Secondary instability of crossflow vortices: validation of the stability theory by direct numerical simulation. *J. Fluid Mech.* **583**, 229–272.

Brockhaus, M.W., Sescu, A., Es-Sahli, O. & Hattori, Y. 2024 Breakdown of Görtler vortices in high-speed boundary layer flows: a DNS study. In *AIAA Aviation Forum and ASCEND 2024*. *AIAA paper* 2024-3533. AIAA.

Casacuberta, J., Groot, K.J., Hickel, S. & Kotsonis, M. 2022 Secondary instabilities in swept-wing boundary layers: direct numerical simulations and biglobal stability analysis. In *AIAA Scitech 2022 Forum*. *AIAA paper* 2022-2330. AIAA.

Chang, C.-L. & Malik, M. 1994 Oblique-mode breakdown and secondary instability in supersonic boundary layers. *J. Fluid Mech.* **273**, 323–360.

https://doi.org/10.1017/jfm.2026.11620 Published online by Cambridge University Press

CHEN, J., DONG, S., CHEN, X., YUAN, X. & XU, G. 2021 Stationary cross-flow breakdown in a high-speed swept-wing boundary layer. *Phys. Fluids* **33** (2), 024108.
CHEN, X., CHEN, J., DONG, S., XU, G. & YUAN, X. 2020 Stability analysises of leeward streamwise vortices for a hypersonic yawed cone at 6 degree angle of attack. *Acta Aerodyn. Sin.* **38** (2), 299–307.
CHEN, X., DONG, S., TU, G., YUAN, X. & CHEN, J. 2022 Boundary layer transition and linear modal instabilities of hypersonic flow over a lifting body. *J. Fluid Mech.* **938**, A8.
CHEN, X., DONG, S., TU, G., YUAN, X. & CHEN, J. 2023 Global stability analyses of Mack mode on the windward face of a hypersonic yawed cone. *Phys. Rev. Fluids* **8** (3), 033903.
CHEN, X., HUANG, G.L. & LEE, C.B. 2019 Hypersonic boundary layer transition on a concave wall: stationary Görtler vortices. *J. Fluid Mech.* **865**, 1–40.
CHEN, X., ZHU, Y. & LEE, C. 2017 Interactions between second mode and low-frequency waves in a hypersonic boundary layer. *J. Fluid Mech.* **820**, 693–735.
CHU, B.-T. 1965 On the energy transfer to small disturbances in fluid flow (Part I). *Acta Mechanica* **1**, 215–234.
CRAIG, S. & SARIC, W. 2016 Crossflow instability in a hypersonic boundary layer. *J. Fluid Mech.* **808**, 224–244.
DI GIOVANNI, A. & STEMMER, C. 2018 Cross-flow-type breakdown induced by distributed roughness in the boundary layer of a hypersonic capsule configuration. *J. Fluid Mech.* **856**, 470–503.
VAN DRIEST, E.R. 1951 Turbulent boundary layer in compressible fluids. *J. Aeronaut. Sci* **18** (3), 145–160.
FEDOROV, A. & EGOROV, I. 2022 Instability of the attachment line boundary layer in a supersonic swept flow. *J. Fluid Mech.* **933**, A26.
GUO, P., HAO, J. & WEN, C.-Y. 2023 Interaction and breakdown induced by multiple optimal disturbances in hypersonic boundary layer. *J. Fluid Mech.* **974**, A50.
HARTMAN, A., HADER, C. & FASEL, H. 2021 Nonlinear transition mechanism on a blunt cone at Mach 6: oblique breakdown. *J. Fluid Mech.* **915**, R2.
HERBERT, T. 1988 Secondary instability of boundary layers. *Annu. Rev. Fluid Mech.* **20**, 487–526.
HIEJIMA, T. 2017 Streamwise vortex breakdown in supersonic flows. *Phys. Fluids* **29** (5), 054102.
HUNTLEY, M. & SMITS, A. 2000 Transition studies on an elliptic cone in Mach 8 flow using filtered Rayleigh scattering. *Eur. J. Mech. B/Fluid* **19** (5), 695–706.
JAHANBAKHSHI, R. & ZAKI, T. 2019 Nonlinearly most dangerous disturbance for high-speed boundary-layer transition. *J. Fluid Mech.* **876**, 87–121.
KACHANOV, Y.S. 1994 Physical mechanisms of laminar-boundary-layer transition. *Annu. Rev. Fluid Mech.* **26**, 411–482.
KOSTAK, H. & BOWERSOX, R. 2021 Preflight ground test analyses of the boundary layer transition (BOLT) flight geometry. *J. Spacecr. Rockets* **58** (1), 67–77.
LI, F., CHOUDHARI, M. & DUAN, L. 2017 Stationary crossflow breakdown due to interaction between secondary instabilities. In *47th AIAA Fluid Dynamics Conference*. *AIAA paper* 2017-4302. AIAA.
LI, F., CHOUDHARI, M. & PAREDES, P. 2020*a* Streak instability analysis on BOLT configuration. In *AIAA Aviation 2020 Forum*. *AIAA paper* 2020-3028. AIAA.
LI, F., CHOUDHARI, M. & PAREDES, P. 2022 Secondary instability of Görtler vortices in hypersonic boundary layer over an axisymmetric configuration. *Theor. Comput. Fluid Dyn.* **36** (2), 205–235.
LI, X., CHEN, J., HUANG, Z., YANG, Q. & XU, G. 2020*b* Stability analysis and transition prediction of streamwise vortices over a yawed cone at Mach 6. *Phys. Fluids* **32** (12), 124110.
LI, X., FU, D. & MA, Y. 2008 Direct numerical simulation of hypersonic boundary-layer transition over a blunt cone. *AIAA J.* **46** (11), 2899–2913.
LIU, S., YUAN, X., LIU, Z., YANG, Q., TU, G., CHEN, X., GUI, Y. & CHEN, J. 2021 Design and transition characteristics of a standard model for hypersonic boundary layer transition research. *Acta Mechanica Sin.* **37** (11), 1637–1647.
MALIK, M., LI, F., CHOUDHARI, M. & CHANG, C.-L. 1999 Secondary instability of crossflow vortices and swept-wing boundary-layer transition. *J. Fluid Mech.* **399**, 85–115.
MOYES, A., BEYAK, E., KOCIAN, T. & REED, H. 2019 Accurate and efficient modeling of boundary-layer instabilities. In *AIAA Scitech 2019 Forum*. *AIAA paper* 2019-1907. AIAA.
MOYES, A., PAREDES, P., KOCIAN, T. & REED, H. 2017 Secondary instability analysis of crossflow on a hypersonic yawed straight circular cone. *J. Fluid Mech.* **812**, 370–397.
MULLEN, C., TURBEVILLE, F., REED, H. & SCHNEIDER, S. 2019 Computational and experimental boundary-layer stability analysis on a hypersonic finned cone. In *AIAA Scitech 2019 Forum*. *AIAA paper* 2019-1381. AIAA.
PAREDES, P., CHOUDHARI, M. & LI, F. 2017 Instability wave-streak interactions in a supersonic boundary layer. *J. Fluid Mech.* **831**, 524–553.

https://doi.org/10.1017/jfm.2026.11620 Published online by Cambridge University Press

PAREDES, P., CHOUDHARI, M. & LI, F. 2019 Instability wave-streak interactions in a hypersonic boundary layer at flight conditions. *J. Fluid Mech.* **858**, 474–499.
PAREDES, P., GOSSE, R., THEOFILIS, V. & KIMMEL, R. 2016 Linear modal instabilities of hypersonic flow over an elliptic cone. *J. Fluid Mech.* **804**, 442–466.
PAREDES, P., SCHOLTEN, A., CHOUDHARI, M. & LI, F. 2021 Hypersonic boundary-layer transition on blunted cones at angle of attack. In *AIAA Scitech 2021 Forum*. *AIAA paper* 2021-2886. AIAA.
PARK, J. & ZAKI, T.A. 2019 Sensitivity of high-speed boundary-layer stability to base-flow distortion. *J. Fluid Mech.* **859**, 476–515.
PECK, M., GROOT, K. & REED, H. 2024 Boundary-layer instability on a highly swept fin on a cone at Mach 6. *J. Fluid Mech.* **987**, A13.
REN, J. & KLOKER, M. 2022 Instabilities in three-dimensional boundary-layer flows with a highly non-ideal fluid. *J. Fluid Mech.* **951**, A9.
REN, J., WU, Y., MAO, X., WANG, C. & KLOKER, M. 2025 Sensitivity of three-dimensional boundary layer stability to intrinsic uncertainties of fluid properties: a study on supercritical CO_2. *J. Fluid Mech.* **1007**, A7.
SCHMID, P. & HENNINGSON, D. 2012 *Stability and Transition in Shear Flows*, Applied Mathematical Sciences, vol. 142. Springer.
SIVASUBRAMANIAN, J. & FASEL, H. 2014 Numerical investigation of the development of three-dimensional wavepackets in a sharp cone boundary layer at Mach 6. *J. Fluid Mech.* **756**, 600–649.
SIVASUBRAMANIAN, J. & FASEL, H. 2015 Direct numerical simulation of transition in a sharp cone boundary layer at Mach 6: fundamental breakdown. *J. Fluid Mech.* **768**, 175–218.
SU, C., LI, G. & HAN, Y. 2024 Breakdown mechanisms induced by stationary crossflow vortices in hypersonic three-dimensional boundary layers. *Phys. Fluids* **36** (7), 074118.
THOME, J., KNUTSON, A. & CANDLER, V. 2019 Boundary layer instabilities on BOLT subscale geometry. In *AIAA Scitech 2019 Forum*. *AIAA paper* 2019-0092. AIAA.
TUFTS, M., BORG, M., BISEK, N. & KIMMEL, R. 2022 High-fidelity simulation of HIFiRE-5 boundary-layer transition. *AIAA J.* **60** (4), 2039–2050.
TURBEVILLE, F. & SCHNEIDER, S. 2019 Transition on a cone with a highly-swept fin at Mach 6. In *AIAA Aviation 2019 Forum*. *AIAA paper* 2019-3217. AIAA.
WANG, H.P., CHEN, X., TU, G.H., WAN, B.B. & CHEN, J.Q. 2024 Stabilities and transition of a hypersonic boundary layer with three-dimensional distributed roughnesses. *Phys. Fluids* **36** (9), 094106.
WANG, Q., XIANG, X., DONG, S., YUAN, X., CHEN, J. & CHEN, X. 2023 Wall temperature effects on the hypersonic boundary-layer transition over an inclined, blunt cone. *Phys. Fluids* **35** (2), 024107.
WANG, Y., YANG, Y., YANG, G. & LIU, C. 2017 DNS study on vortex and vorticity in late boundary layer transition. *Commun. Comput. Phys.* **22** (2), 441–459.
WASSERMANN, P. & KLOKER, M. 2002 Mechanisms and passive control of crossflow-vortex-induced transition in a three-dimensional boundary layer. *J. Fluid Mech.* **456**, 49–84.
WASSERMANN, P. & KLOKER, M. 2003 Transition mechanisms induced by travelling crossflow vortices in a three-dimensional boundary layer. *J. Fluid Mech.* **483**, 67–89.
WHEATON, B., BERRIDGE, D., WOLF, T., STEVENS, R. & MCGRATH, B. 2018 Boundary layer transition (BOLT) flight experiment overview. In *2018 Fluid Dynamics Conference*. *AIAA paper* 2018-2892. AIAA.
WU, X., STEWART, P. & COWLEY, S. 2007 On the catalytic role of the phase-locked interaction of Tollmien–Schlichting waves in boundary-layer transition. *J. Fluid Mech.* **590**, 265–294.
XU, G., CHEN, J., LIU, G., DONG, S. & FU, S. 2019 The secondary instabilities of stationary cross-flow vortices in a Mach 6 swept wing flow. *J. Fluid Mech.* **873**, 914–941.
YANG, L., LI, X. & LIU, H. 2025 Direct numerical simulation of hypersonic boundary layer transition over a lifting body at different angles of sideslip. *Phys. Fluids* **37** (3), 034123.
YAO, J. & HUSSAIN, F. 2022 Vortex reconnection and turbulence cascade. *Annu. Rev. Fluid Mech.* **54**, 317–347.
ZHANG, L., CHEN, X., LIU, S., WANG, Q., DONG, S., DUAN, M. & CHEN, J. 2025 Transition front prediction for the HyTRV model based on multi-dimensional stability theories. *Adv. Aerodyn.* **7** (1), 1–21.
ZHANG, L., DONG, S., LIU, S., YUAN, X., CHEN, J. & CHEN, X. 2022 Stability analysis of streamwise vortices over a blunt inclined cone under a hypersonic flight condition. *Phys. Fluids* **34** (7), 074107.
ZHOU, T., LIU, Z., LU, Y. & YAN, C. 2023 Interactions between oblique second mode and oblique waves in a high-speed boundary layer. *J. Fluid Mech.* **973**, A27.

https://doi.org/10.1017/jfm.2026.11620 Published online by Cambridge University Press